

PAPER NEUTRON AND X-RAY SCATTERING APPLIED TO CONDENSED MATTER PHYSICS

Future trends in synchrotron science at NSLS-II

To cite this article: John Hill *et al* 2020 *J. Phys.: Condens. Matter* **32** 374008

View the [article online](#) for updates and enhancements.



IOP | ebooks™

Bringing together innovative digital publishing with leading authors from the global scientific community.

Start exploring the collection—download the first chapter of every title for free.

Future trends in synchrotron science at NSLS-II

John Hill^{1,5}, Stuart Campbell¹ , Gabriella Carini², Yu-Chen Karen Chen-Wiegart^{1,3}, Yong Chu¹, Andrei Fluerașu¹, Masafumi Fukuto¹, Mourad Idir¹, Jean Jakoncic¹, Ignace Jarrige¹, Peter Siddons¹, Toshi Tanabe¹ and Kevin G Yager⁴ 

¹ National Synchrotron Light Source II (NSLS-II), Brookhaven National Laboratory, Upton, NY, United States of America

² Instrumentation Division (IO), Brookhaven National Laboratory, Upton, NY, United States of America

³ Materials Science & Chemical Engineering, Stony Brook University, Stony Brook, NY, United States of America

⁴ Center for Functional Nanomaterials (CFN), Brookhaven National Laboratory, Upton, NY, United States of America

E-mail: hill@bnl.gov

Received 9 January 2020

Accepted for publication 28 February 2020

Published 18 June 2020



CrossMark

Abstract

In this paper, we summarize briefly some of the future trends in synchrotron science as seen at the National Synchrotron Light Source II, a new, low emittance source recently commissioned at Brookhaven National Laboratory. We touch upon imaging techniques, the study of dynamics, the increasing use of multimodal approaches, the vital importance of data science, and other enabling technologies. Each are presently undergoing a time of rapid change, driving the field of synchrotron science forward at an ever increasing pace. It is truly an exciting time and one in which Roger Cowley, to whom this journal issue is dedicated, would surely be both invigorated by, and at the heart of.

Keywords: synchrotron x-ray, imaging, inelastic scattering, coherent scattering

(Some figures may appear in colour only in the online journal)

Introduction

Synchrotron science is an extremely fast moving field of science. Driven by increases in the brightness of the sources, and by improvements in optics, in detectors, and in data handling, the field is almost routinely transformed every few years in terms of what kinds of experiments can be performed. For example, the brightness of sources have increased at a rate that has far exceeded even the rate at which transistor density has increased, so-called Moore's law, over the same period. In this article, we seek to point out some of the future trends in synchrotron science as seen at National Synchrotron Light Source II (NSLS-II) at Brookhaven National Laboratory. We note that this is not intended to be a review of the field, rather a snapshot of what is currently happening at NSLS-II.

⁵ Author to whom any correspondence must be addressed.

In section 1, we address imaging, including scanning, full field, and diffractive imaging. In section 2, we discuss the study of dynamics, both in the time domain and in the energy domain. Section 3 addresses the trend toward multimodal experiments, i.e. combining data from multiple different techniques. Section 4 discusses the trends in data and computer science. Finally, section 5 looks at some enabling technologies including optics, detectors, and insertion devices.

1. Imaging

The significant enhancement of source brightness has allowed for the construction of x-ray beamlines for nanoscale imaging with ever more sophisticated capabilities. Nanoscale x-ray imaging can be categorized into three types: scanning microscopy, full-field microscopy, and coherent diffractive imaging.

X-ray nanoprobe typically utilize scanning microscopy, where a sample is scanned through a nanobeam and signals produced from the sample are collected. The collected signals are transformed into images mapping various properties of the sample, such as element distribution, morphology, chemical states, or crystalline ordering. The advantage of scanning microscopy resides on its capability to correlate different structural or chemical properties of the sample, also referred to as a multimodal imaging capability [1, 2]. Several different types of nanofocusing optics can be used to produce a focused beam, based on specific instrument or scientific requirements. The size of the beam and its flux are the key performance parameters of x-ray nanoprobe. Achieving the diffraction-limited focus size requires coherent illumination on the focusing optic by the x-ray beam. Due to this requirement, the flux over the smallest focused beam for a specific nanoprobe scales with coherent flux of the synchrotron source or the source brightness. In practice, certain measurements prefer higher focused flux over a smaller focus size. In order to facilitate an easy way to trade the focus size with the flux, an elaborate optical scheme is employed so that the degree of coherence over the focusing optic is controlled by manipulating the amount of phase space volume of the source that is transmitted through a secondary source aperture [1, 3, 4]. Due to the complexity of the photon delivery scheme, a typical nanoprobe beamline is usually much longer than other beamlines and, often, is equipped with a dedicated satellite building for better vibration isolation and higher temperature stability for its endstation [1, 3, 4].

Nanoscale full-field microscopy is usually implemented using a transmission x-ray microscope (TXM) though a projection microscope can also be used [3]. A TXM consists of condenser and objective optics plus an imaging detector system. The condenser optics focuses x-rays onto a sample, and the transmitted and scattered x-rays are imaged by the objective optics onto the imaging system. Consequently, an absorption image of the sample is captured at once. Sensitivity to element specificity and oxidation states is achieved by collecting a series of 2D images across an absorption edge [5–7]. Zernike contrast can be employed to enhance the detection sensitivity of low-Z elements [8, 9]. Both TXMs and nanoprobe serve an important role in nanoscale imaging. Unlike a nanoprobe, a TXM is based on incoherent imaging. Consequently, effects due to high coherence such as speckles are problematic for a TXM, since these cannot be removed by simple flat-field correction. On the other hand, the imaging throughput of a TXM is determined not by source brightness alone but also by optimization of the phase space available from the source. For this reason, a wiggler source may be a better choice than an undulator source. One disadvantage of full-field imaging is that the desired signal overlaps with the bright background due to the direct beam, which limits the detection sensitivity of this technique, whereas, the detection sensitivity of scanning microscopy can easily exceed one part per million. An obvious advantage of full-field microscopy is its imaging throughput, which is typically many orders of magnitude faster than scanning microscopy. Consequently, it is ideally suited for the study of dynamics or 3D investigations.

Coherent diffractive imaging (CDI) does not require either an objective or condensing lens [10], although the latter is useful to increase detection sensitivity. A CDI microscope does not form an image directly, instead it collects the far-field scattering from the sample in an area detector. This dataset is used as input to the solution of an inverse problem, which requires iterative reconstruction [11]. It is generally assumed that the x-rays interact with matter only once within the sample, allowing the complex image to be interpreted as a refraction index map, where the imaginary component is responsible for the absorption contrast and the real is responsible for phase retardation of the illuminating field [12]. In some instances, this map can be used to determine density or chemical composition of spatially resolved regions within the sample [13]. CDI can be employed in either a full-field [10] or a scanning mode, the latter better known as ptychography [14, 15]. In the former, CDI is more dose efficient [16] than traditional or lens-based microscopy and, in the latter, the image resolution does not depend on the size of the focused beam as it would in a nanoprobe. CDI can also employ a Bragg diffraction pattern, because the image is algorithmically recovered as the solution to an inverse problem, which can be applied to the intensity distribution around any Bragg peak [17, 18]. In this case, the image formed is still an exit-surface snapshot. However, the phase contains an additional dependency upon the deformation of the crystalline specimen. The requirements on the illumination of the sample, that the illumination be coherent and monochromatic, limit the ultimate speed of data acquisition, and these constraints on the method are under investigation [19, 20]. CDI is a form of microscopy that overcomes the resolution limit of x-ray lenses but at the expense of conducting a more rigorous experiment and the need to solve an inverse problem.

The hard x-ray nanoprobe (HXN) beamline at the NSLS-II is optimized for high-resolution scanning microscopy and is equipped with the state-of-the-art x-ray microscope [1, 21]. The experimental hutch is located within a satellite building to achieve vibration isolation and temperature stability. The endstation x-ray microscope called Nano-MII (Nanoscale Multimodal Imaging Instrument) is specifically designed to achieve high positioning stability by employing interferometric positioning feedback and minimizing heat generation from the nanostages and their interpolators. At the sample position, the vibration amplitude is less than 0.5 nm RMS over its resonant frequencies [21].

A unique feature of Nano-MII is the choice of multilayer Laue lenses (MLLs) or a zoneplate (ZP) as the nanofocusing optic, depending on experimental needs. The MLLs produce a focused beam of 12 nm, operating at 12–20 keV. The zoneplate focuses down to ~ 30 nm with an operating range of 6–15 keV. Nano-MII performs multimodal imaging by detecting x-ray signals due to fluorescence, phase-contrast, and/or diffraction [1, 2]. The images in figures 1(a)–(c) show typical multimodal imaging results obtained from non-crystalline samples using a pair of MLLs as the focusing optics. The data are collected from a cluster of self-assembled Au nanoparticles with a cubical shape of 40 nm in size. Figure 1(a) shows the elemental map produced from the XRF signal. The 0th-order diffraction

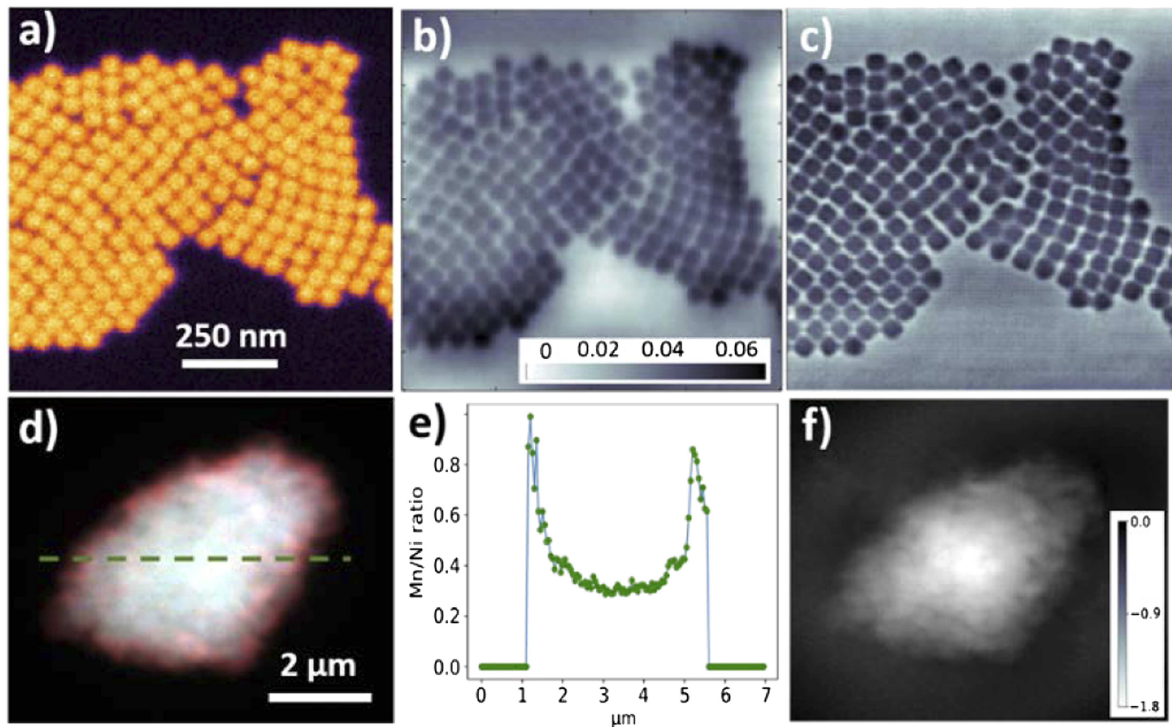


Figure 1. Multimodal imaging capability at the HXN beamline at NSLS-II. (a) Au fluorescence image, (b) phase image determined from DPC analysis, and (c) phase image determined from ptychography analysis. (a)–(c) are simultaneously obtained from self-assembled Au nanoparticles of about 40 nm in size using MLLs as focusing optics. (d) Element distribution map (red = Mn, green = Co and blue = Ni) obtained from a LiNiMnCo core–shell structured battery sample. (e) Relative composition ratio between Mn and Ni along the dotted line shown in (d). (f) Phase image determined from ptychography analysis; (d)–(f) are obtained using a zoneplate as a focusing optic.

pattern produced by the transmitted beam is analyzed via differential phase contrast (DPC) imaging [22] and ptychography, respectively in figures 1(b) and (c).

Retrieving absorption and phase maps of the sample for DPC imaging utilizes a deterministic integration process [21] with a spatial resolution determined by the size of the nanobeam. The XRF and DPC images in figures 1(a) and (b) show a spatial resolution of about 12 nm, sufficient to characterize the ordering of the nanoparticle assembly with an inter-particle gap of ~ 10 nm. The same dataset can also be analyzed using ptychography reconstruction to produce a phase map, figure 1(c), with an estimated spatial resolution of about 8.5 nm.

Figures 1(d) and (e) show multimodal imaging results obtained using a zoneplate as the focusing optic, with an FWHM focused beam size of about 60 nm. The data were obtained from a LiNiMnCo core–shell structured battery material. A combination of fluorescence and ptychography imaging produces a comprehensive structural analysis of element distribution with moderate resolutions and the nanostructure with higher resolutions. Calibrated XRF measurements produce quantitative composition maps (figures 1(d) and (e)), while the high resolution ptychography image (figure 1(f) with a resolution of about 19 nm) reveals internal nanostructure due to agglomeration of primary particles within the secondary core–shell particle of several microns in size. A typical multimodal imaging measurement at the HXN beamline

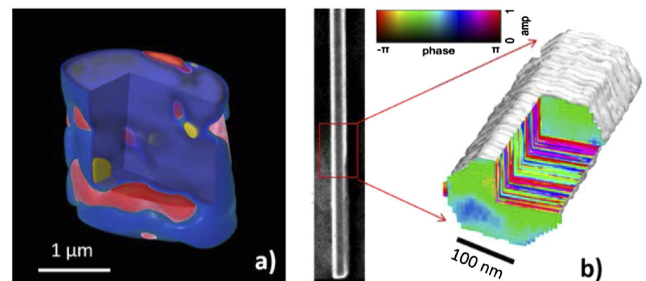


Figure 2. Examples of 3D imaging capability of the HXN beamline at NSLS-II. (a) 3D element distribution within a mixed ion-electronic conducting ceramic-based membrane sample, analyzed by a scanning XRF tomography. Three different material phases are identified: CGO (blue), CFO (red) and GFCCO (yellow). (b) 3D stacking fault distribution within an $\text{In}_{0.86}\text{Ga}_{0.14}\text{As}$ nanowire sample, analyzed by 3D Bragg ptychography. The insert on the left is the SEM image of the nanowire, indicating approximate position of the measurement.

consists of 200×200 pixels with a 50 nm dwell time per pixel, which takes about 40 min using a continuous fly-scan. A typical ptychography reconstruction time for such dataset using the online GPU cluster at the beamline is less than 5 min [23–26].

Multi-dimensional imaging can be achieved by collecting image stacks as a function of energy for chemical imaging, projection angles for 3D tomographic analysis or diffraction angles for 3D Bragg ptychography. Figure 2(a) shows an XRF

tomography analysis performed on a mixed ion-electronic conducting (MIEC) ceramic-based membrane sample, produced by sintering two precursor materials phases $\text{Ce}_{0.8}\text{Gd}_{0.2}\text{O}_{2-x}$ (CGO) and CoFe_2O_4 (CFO) [27]. The reconstructed volumetric data show an additional phase (yellow), referred to as GFCCO phase, segregated from the initial phases due to high temperature sintering, and believed to have significant influence on the electronic and ionic transport properties of this material [26]. In addition, the collected 3D data have sufficient sensitivity to analyze the variation of the metal concentrations, so that element-specific diffusion at the grain boundary can be investigated. Figure 2(b) shows the 3D Bragg ptychography result obtained from an $\text{In}_{0.86}\text{Ga}_{0.14}\text{As}$ nanowire sample [28], which visualizes both strain distribution and stacking fault defects in the nanowire. Imperfect atomic layer stacking sequence along the c -axis (i.e., the growth direction of the nanowire) produces the six-fold symmetry corresponding to the hexagonal wurtzite structure. By analyzing a reflection sensitive to stacking-faults, stacking fault defects are imaged with a resolution better than 3 nm along the axial direction.

Bragg ptychography as a part of nanoprobe's multimodal imaging capabilities is a highly effective tool for imaging strain and crystalline defects, providing a simple way to correlate the result with other imaging modalities such as fluorescence. However, when complementary information is not required at high resolution and the sample is micron-sized or smaller, traditional Bragg Coherent Diffractive Imaging (CDI) provides the same information faster and with a lower radiation dose, since it does not require scanning the sample. These considerations are particularly important for dynamics or for time-resolved investigations. Additionally, a Bragg CDI experiment often exhibits relaxed requirements on the sample environment, e.g., long working distances and compatibility with *operando* or *in situ* cells, and the experimental convenience of working with micron-scale x-ray beams. The ideal experimental configuration for conducting CDI measurements involves tailoring the phase-space of the beam to illuminate the sample with a coherent and stable wavefront. As such, the traditional approach of defining and then filtering a secondary source does not provide the best-possible illumination of the sample. At NSLS-II, a new beamline is under development to maximize experimental throughput by providing an illumination such that the x-ray beam size and coherence properties can be independently varied. This new CDI beamline will facilitate the imaging of micron-sized and smaller crystals as quickly as possible. The capability to conduct Bragg CDI on operating devices is expected to have a significant impact on a wide variety of topics areas. Fundamental questions in materials science, for example, nano-scale studies of ferroelectric and mechanical properties, will be addressable. Studies of energy storage and conversion materials will reveal structural changes and the onset of failure in *operando* devices.

The full-field x-ray imaging (FXI) beamline at the NSLS-II forms full-field imaging using a transmission x-ray microscope (TXM) [29, 30]. The most powerful capability of the FXI beamline is its imaging speed. For most samples, an

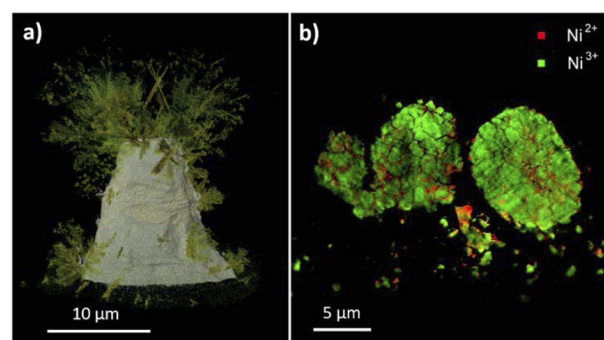


Figure 3. 3D imaging capabilities of the FXI beamline at NSLS-II. (a) *In situ* growth of Ag dendrite from a solution captured using a rapid TXM tomography measurement. (b) 3D oxidation distribution of Ni^{2+} and Ni^{3+} analyzed using XANES tomography with 56 energy points across the Ni K-edge.

acquisition time of 10–50 ms is appropriate for producing a high-contrast 2D image with a $40\ \mu\text{m} \times 40\ \mu\text{m}$ field of view (containing 2000×2000 pixels) and 30 nm resolution. This is achieved by matching the phase space of the source with the incoherent imaging requirement. An objective optic with a spatial resolution of 30 nm has a numerical aperture (NA) of about 2.6 mrad (i.e. total angular spread of 5.2 mrad). If the objective optic has a field of view of $40\ \mu\text{m}$, the corresponding imaging system uses a total phase space of about $208\ \mu\text{m mrad}$. Undulators have significantly smaller phase space (i.e. x-ray source size times divergent angle) and bending magnet sources have poor on-axis brightness. The NSLS-II's damping wiggler is an ideal source delivering 10^{13} ph/s over the field of view at the sample.

Short acquisition times enable investigation of dynamical systems in the temporal range of milliseconds to tens of seconds by either taking fast 2D snapshots or performing 3D tomography measurements. Figure 3(a) shows a 3D snapshot of the electrolyte/electrode interface during Ag dendrite growth on the Cu electrode in an electrolyte. The data were collected while the sample was continuously rotating at a rate of $3^\circ\ \text{s}^{-1}$ with the exposure time of 20 ms per projection. The reconstructed 3D volume, using a dataset consisting of 1060 projections collected over a total of 1 min, shows well-defined dendrite feature down to a minimum feature size of about 45 nm [30]. A significant majority of hard energy TXM applications today focus on visualizing oxidation states associated with electrochemical reactions by combining XANES measurements [6, 7, 31]. This so-called XANES tomography measurement produces a large-size four-dimensional dataset (tomography at multiple energy points) and can naturally add significant data collection time. Figure 3(b) shows a 3D oxidation map of Ni^{2+} and Ni^{3+} , visualizing the electrochemical transformation in a $\text{LiNi}_{0.5}\text{Mn}_{0.3}\text{Co}_{0.2}\text{O}_2$ (NMC) battery material. This XANES tomography measurement, consisting of a total of 22 456 projections (401 projections at 56 energy points with each projection containing 1080×1280 pixels), took a total collection time of less than 90 min, which is unprecedentedly fast when compared with other nanoscale imaging methods.

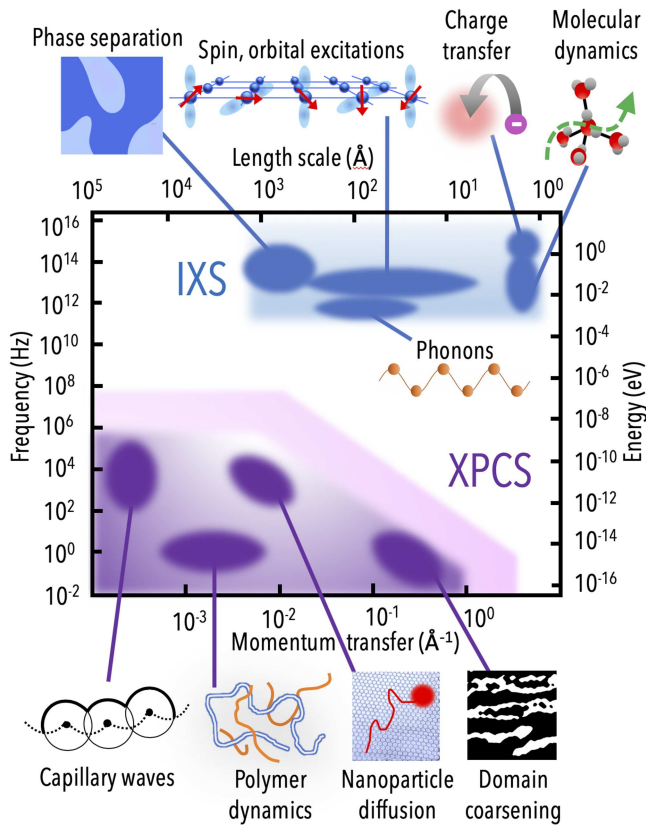


Figure 4. Physical processes and phenomena that can be probed using IXS and XPCS in the energy and time domains. The pink band for XPCS represents upcoming improvement in frequency and momentum in coming years.

2. Dynamics

While most scattering techniques measure structural information averaged over large ensembles of scatterers, as quantified by the static structure factor $S(q)$, new classes of experiments measuring dynamical information have become feasible with the tremendous increase in source brightness. Among them, inelastic x-ray scattering (IXS) measures the frequency-dependent dynamic structure factor $S(q, \omega)$ and x-ray photon correlation spectroscopy (XPCS) measures the Fourier transform of this dynamic structure factor, $S(q, t)$. IXS and XPCS are able to provide dynamical information on a combination of time/frequency and length scales that are inaccessible to other techniques (figure 4).

2.1. Time-domain measurements

Coherent X-ray scattering was first demonstrated by Sutton and collaborators [32] who showed that by sufficient collimation one can observe interference patterns a.k.a. ‘speckle’ from static samples inserted in a partially coherent beam. A coherent scattering experiment requires thus a ‘trade off’ between flux and coherence. The flux of x-ray photons going through a given slit or pinhole used to define a coherent or partially coherent beam scales linearly with the source brightness.

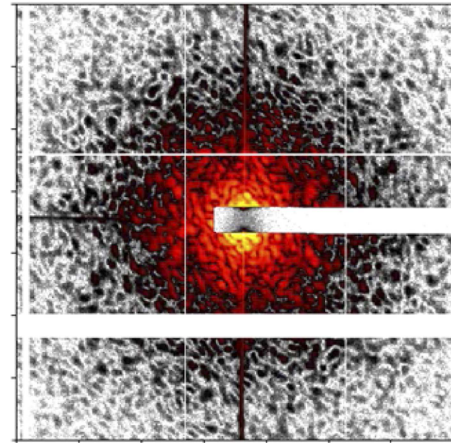


Figure 5. Example of a speckle pattern obtained at the NSLS-II coherent hard x-ray (CHX) beamline from a static sample of Au ‘nanodots’ on a silicon nitride membrane.

The key aspect regarding coherent scattering is that, if the scatterers fluctuate, then the speckle patterns will fluctuate in time. In this case, a time auto-correlation function of the q -dependent scattered intensity can be related to the dynamic structure factor $S(q, t)$. This technique, XPCS, can be used to probe equilibrium and out-of-equilibrium dynamics and to characterize dynamical heterogeneities on a wide range of time- and length-scales (figure 5) which are difficult or impossible to probe with other techniques. For some recent reviews of the XPCS technique, see [33, 34] and references therein.

2.1.1. Current state-of-the-art. The development of XPCS over the past 20+ years features a continuous increase toward faster time scales. While the first demonstrations of the technique [35, 36] were carried with total partially coherent fluxes of 10^7 to 10^8 ph/s to reach time scales of the order of tens to hundreds of seconds, the most recent experiments have reached millisecond and sub-millisecond time scales [37, 38]. This development was enabled by the fact that the signal-to-noise of the XPCS measurements scales linearly in source brightness but only with the square root of the shortest acquisition time. Figure 6 shows the dynamic structure factor measured recently at the NSLS-II CHX beamline with a coherent flux exceeding 10^{11} ph/s at a photon energy of 9.65 keV. The sample used in these tests was an associative polymer network prepared in B Olsen’s lab [39].

One of the most important developments enabling XPCS is that of fast area detectors with single photon sensitivity [40]. The use of pixel array detectors [41, 42] maximizes the signal-to-noise by averaging the correlation functions over thousands of pixels and enables out-of-equilibrium, time dependent studies through two-time correlation functions [43].

XPCS combined with a small angle scattering (SAXS) geometry has become an invaluable tool for quantifying and understanding bulk dynamics in a variety of complex soft materials including, but not being limited to, block copolymers [44], charge-stabilized suspensions [45], colloidal glasses [46, 47] and colloidal gels [48, 49]. The connection

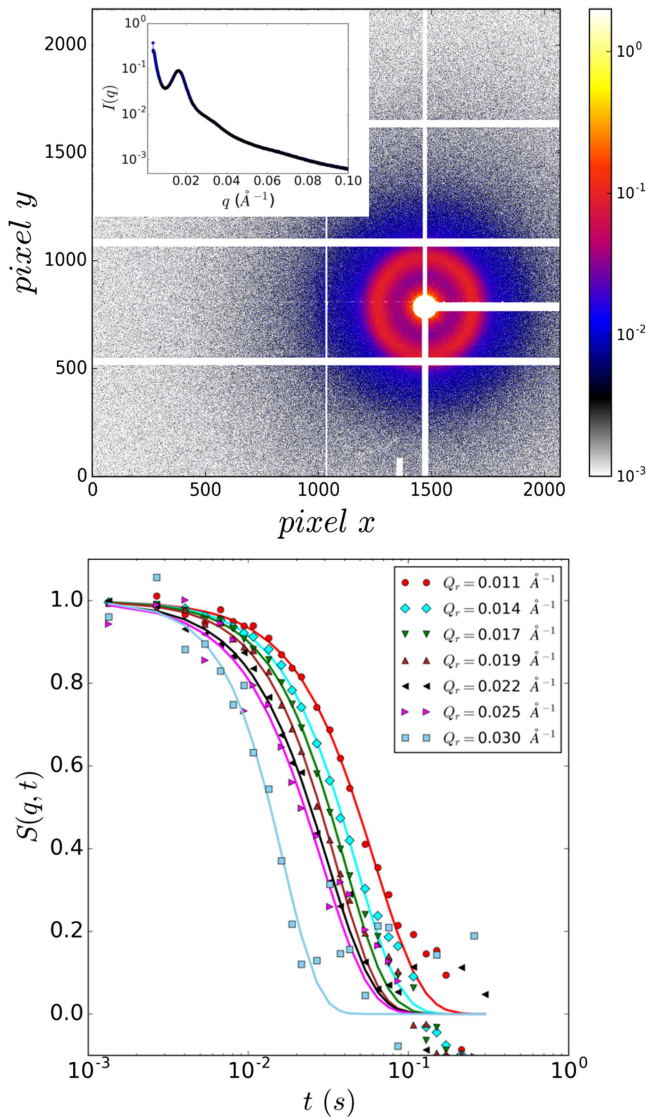


Figure 6. Top: single frame speckle pattern and circular averaged static scattered intensity $I(q)$ from an associative network of polymers; bottom: dynamic structure factor $S(q,t)$ revealing millisecond fluctuations (dynamics) on length scales ranging from $\sim 20\text{--}60$ nm.

between nanoscale dynamics and rheology was studied in a number of experiments on colloidal fluids under continuous flow [50], homogeneous shear [51] and oscillatory shear [52].

XPCS has also been used in grazing incidence SAXS as a surface sensitive probe to study dynamics at polymer surfaces and interfaces [53, 54], capillary waves in polymer films and *in situ* studies of dynamics during thin film growth [55].

One of the most important capabilities of hard x-rays is their ability to access atomic and molecular length scales. The use of XPCS in a wide-angle scattering geometry was pioneered by Sutton and collaborators through studies of equilibrium critical dynamics [35] and dynamical scaling of domain coarsening during first order phase transitions [56, 57] in binary alloys. Other examples of wide angle XPCS include, but are not limited to, surface reconstruction in single crystalline

materials [58], antiferromagnetic domain fluctuations [59] and studies of atomic fluctuations in network glasses and single crystals.

The list of experiments described above is far from a complete overview of the advances enabled by XPCS over the last 20 years but covers some of the important aspects of these developments. Many of the studies have found evidence of complex dynamics going beyond simple Brownian diffusion [60].

2.1.2. Future trends. While existing facilities like the hard and soft x-ray coherent scattering beamlines at NSLS-II provide world-leading fluxes of coherent beams, the future is even brighter with upcoming diffraction-limited storage rings upgrade projects at the ESRF and APS. These new facilities will provide an increase in brightness of two orders of magnitude relative to NSLS-II, enabling, in principle, storage ring XPCS experiments covering time scales from microseconds or faster to hours. These new instruments will complement capabilities offered by IXS, neutron spin echo or coherent scattering at free electron laser facilities.

In order to take full advantage of the current and future capabilities, a continuous improvement in the detector technology will be required. New devices such as an NSLS-II detector development [38] based on the vertically integrated photon imaging chip (VIPIC) enable time resolutions up to 20 ns. The coherent scattering experiments at high brightness sources will also increasingly start complementing sequential XPCS from time-series of speckle patterns with ‘single shot’ x-ray photon correlation spectroscopy (XSVS) [61, 62]. By doing so, the dynamic structure factor can be obtained in some cases on time scales faster than the shortest acquisition time that pixel array detectors can sustain in a continuous, sequential mode.

The more intense x-ray beams will also result in faster beam-induced damage. In order to mitigate these effects, the experiments will have to evaluate the maximum allowable doses for individual samples and use those to access the fastest possible time scales in conjunction with controlled attenuation to access slower time scales when needed.

As the XPCS technique becomes more mature, we witness an increasing trend toward more complex sample handling and *in situ* experiments. For example, the new effort started at the NSLS-II CHX beamline on additive manufacturing [63], and the study of the interplay between the nanoscale structure and dynamics and the macroscopic rheological properties of the inks and printed materials. XPCS will also likely provide an increasingly useful experimental tool to the study of *in situ* processes such as thin film growth [64].

As the brighter beams allow access to faster time scales, XPCS experiments will become increasingly relevant to a number of biological dynamical processes such as protein folding in systems where the beam damage can be mitigated by a careful control of the irradiation dose.

With brighter beams and faster detectors, the data rates will very quickly reach hundreds of MB s^{-1} with data volumes of perhaps several TB/day. Data transfer and data analysis by external users at their home institutions will become an

increasingly impractical solution. Facilities will have to provide capabilities for remote data access and advanced analysis methods.

Finally, it should be mentioned that diffraction limited synchrotron sources will provide coherent diffraction speckle patterns with most samples whether this is the purpose of the experiment or not. In some of the cases, this may appear as a nuisance. However, a speckle pattern contains more information than an ensemble averaged incoherent scattering diffraction pattern. X-ray scattering experiments at future sources may start to take advantage of the additional information encoded by the beam coherence through data analysis that will go beyond calculating time autocorrelation functions and the dynamic structure factor. Speckle tracking and evaluation of e.g. velocity profiles or strain [65] is one example of such possible new application.

2.2. Energy domain measurements

Some of the deepest problems in quantum materials are related to collective electronic phenomena, such as high-temperature superconductivity and solid-state topology. Understanding collective electronic excitations at low energies and with sizable momentum transfers produces a challenging requirement of simultaneous high energy resolution and variable momentum transfer. This is met by inelastic x-ray scattering (IXS) [66]. Game-changing improvements in energy resolution and throughput have recently highlighted the sensitivity of IXS to the charge, orbital, and spin degrees of freedom of the electrons [67, 68], and it is now becoming possible to map out the energy–momentum dispersion of these low-energy excitations in a way that is not feasible with optical probes due to the lack of momentum, or with inelastic neutron scattering because of cross-section reasons, or because the samples of interest can often be small single crystals, thin films, or small devices.

2.2.1. Current state-of-the-art. The two central experimental challenges for IXS are the throughput and the energy resolution, as the excitations suffer from a relatively low cross section and they can appear at low energy transfers, overlapping with the tail of the elastic line. These issues are interconnected, as improvements of the energy resolution are often achieved at the cost of throughput. In this subsection, we outline the main design features and the current status of the world-leading instruments in the field.

2.2.1.1. RIXS. Resonant inelastic x-ray scattering (RIXS), which uses incoming photons resonantly tuned to absorption edges, can be used in the soft or hard x-ray energy range depending on the absorption edge of interest. Despite using substantially different equipment, soft and hard x-ray RIXS have both benefited from a sustained worldwide effort to develop new beamlines over the last two decades. This has resulted in a tremendous improvement in resolving power by a factor of 20–30, bringing RIXS to the heart of low-energy physics of quantum materials.

In the soft x-ray regime, RIXS is most often used at the K edge of low-Z elements, the L edge of 3d transition metals

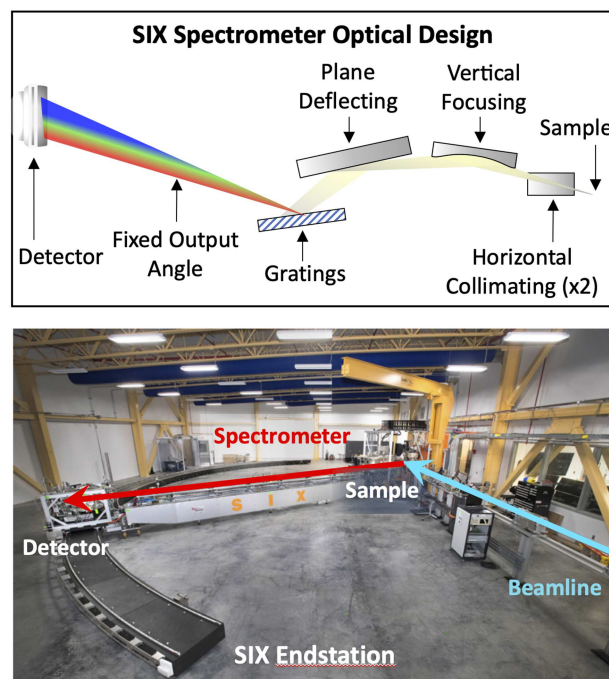


Figure 7. (Top) Optical scheme of the SIX spectrometer. (Bottom) Panoramic view of the downstream end of the SIX beamline and of the 15 m long spectrometer.

(TMs), and the M edge of 4f materials. These edges yield a strong signal and provide direct access to the valence electrons through dipolar coupling with the core hole.

The current highest resolving power for soft x-ray RIXS, 30 000 (30 meV at 1000 eV), is achieved by three beamlines in the world—the soft inelastic x-ray scattering beamline (SIX) at NSLS-II [69, 70], the ID32 beamline at the ESRF [71], and the I21 beamline at Diamond Light Source. In fact, the SIX beamline has recently achieved a world-record resolving power of 45 000 (22 meV at 1000 eV). All three beamlines share similarities in the design of their photon delivery system, based on a varied line spacing (VLS) plane grating monochromator (PGM) with long entrance and exit arms which, for a given resolving power, allows for more efficient (lower line density) gratings to be used. The approaches diverge at the spectrometer, as ID32 and I21 use a conventional optical design based on a spherical grating, while SIX, which has a target ultrahigh resolving power of 70 000 (15 meV at 1000 eV), relies on a Hettrick–Underwood optical scheme (figure 7). This scheme minimizes the range of mechanical movements in order to meet the tight mechanical stability requirements and provides a nearly upright focal plane at the detector to optimize the detection efficiency. Further, while the aberrations are minimized over the entire energy range by changing the height of the detector at ID32 and I21, SIX uses an additional plane deflection mirror to keep the direction of the diffracted beam constant and the detector close to ground level, which is crucial to maintain the required vertical stability at the detector.

RIXS beamlines that operate in the hard x-ray range are routinely used for experiments at the K edge of 3d TMs and the

L edge of 5d TMs and 4f materials. These experiments benefit from significantly wider momentum transfer ranges than soft x-ray RIXS. While K-edge RIXS on 3d TMs suffers from a weak cross-section as the excitations are created indirectly through a shakeup process in the presence of the core hole, hard x-ray RIXS has recently seen a resurgence of activity with the observation of strong signals through a direct process at the L edge of 5d TMs [72]. RIXS studies of the low-energy dynamics of 5d TMs have helped uncover the novel physics brought about by the strong spin-orbit coupling (SOC) of these materials, including SOC-assisted Mott physics [73], Kitaev quantum spin liquid states [74], and topological Weyl semimetal behavior [75].

Hard x-ray RIXS instruments rely on a combination of a double-bounce high-heat load monochromator and a four-bounce high-resolution monochromator for the beamline, and Rowland-type spectrometers based on spherical diced crystal analyzers used in near-backscattering geometry. Because each edge requires different crystal reflections, the energy resolution of hard x-ray RIXS is strongly edge dependent. The current world-leading resolution is 10 meV, achieved at the Ir L₃ edge (11.215 keV) at the 27-ID beamline of the Advanced Photon Source, using a flat quartz spectrometer analyzer combined with a Montel mirror to increase the acceptance of the scattered beam [76]. With the conventional spherical diced analyzer setups, the best resolutions achieved for 5d TMs at 27-ID and at the ID20 beamline at the ESRF range from 25 meV at the Ir L₃ edge, to 50 meV at Os L₃, 90 meV at Ta L₃, and 200 meV at Pt L₃ [77, 78].

2.2.1.2. Hard x-ray NIXS. When detuning the incident energy away from resonance, the cross-section for electronic excitations becomes weaker, but also relatively simpler to interpret as it is directly proportional to the two-particle correlation function (note, here we do not discuss phonon measurements, though the instrumental requirements are similar). This is a distinctive advantage of non-resonant inelastic x-ray scattering (NIXS), which also benefits from the fact that the operating energy can be chosen based solely on energy resolution considerations since there is no need to satisfy resonance conditions. To compensate for the inherently low cross-sections, NIXS spectrometers are equipped with a large number of crystal analyzers, which maximizes the solid angle of detection. BL43XU beamline of SPring-8 [79] is an example of a NIXS beamline. A resolution of 25 meV is achieved by applying a temperature gradient to the analyzers, which introduces a gradient in the lattice constant to correct for the variation of the Bragg angle over the individual analyzers. The rest of the NIXS spectrometers in the world are optimized for x-ray Raman scattering (XRS), which measures shallow core-level x-ray absorption edges using non-resonant hard x-ray beams at medium energy resolutions [80, 81].

2.2.2. Future trends.

2.2.2.1. Drive to 1 meV resolution in soft RIXS Here we describe conceptual approaches to further improve the resolution in soft x-ray RIXS. First, without any significant changes

to the current optical design of the SIX beamline at NSLS-II, 3 meV at 1000 eV can be obtained at the expense of a factor 10 in throughput with moderately higher line-density gratings ($\sim 3000 \text{ mm}^{-1}$) operating in the second order, and with an improvement of the spatial resolution of the detector by a factor of 2. To get to 1 meV gratings with line densities on the order of $4000\text{--}5000 \text{ mm}^{-1}$ operating in fourth–fifth order would be required. The resulting loss in throughput of three orders of magnitude would require significant changes to the optical design. One optical scheme is the matched dispersion beamline/spectrometer design used by the soft x-ray RIXS beamline at the Taiwan Photon Source, which places an energy dispersed image of the exit plane of the monochromator onto the sample, which is then focused by the spectrometer onto the detector in terms of energy loss. This scheme provides a way to increase the incident energy bandwidth by a factor of 10–100, while another factor of 2–3 could be further gained by using multilayer blazed gratings.

2.2.2.2. Spatial resolution. Newer-generation soft x-ray RIXS instruments boast a vertical focus at the sample of one to a few microns, which is required to achieve high energy resolutions, but have a more relaxed horizontal focus. To carry out RIXS imaging will take further improvements of the focusing down to $\sim 100 \text{ nm}$ to access the length scales relevant to quantum materials, such as intrinsic electronic inhomogeneities, artificial nanoscale structures, and some of the local mechanisms that determine the dynamical evolution of quantum states. At the same time, considerable improvements of the spectrometer throughput will also be required. The low emittance and high stability of the beam at NSLS-II provides an opportunity to build a soft x-ray RIXS beamline with a $\sim 100 \text{ nm}$ spot size achieved with, for example, a pair of Kirkpatrick–Baez mirrors. Such a beamline is currently being designed with simultaneous ARPES capabilities.

3. Multimodal synchrotron characterization

3.1. The need for multimodal synchrotron characterization

Scientific and technological advances are the driving forces for developing multimodal synchrotron characterization, with their universal needs to understand complex and heterogeneous systems. Multimodal synchrotron characterization is defined here as utilizing techniques across multiple beamlines at synchrotron light sources, and/or in combining synchrotron-based techniques with other modalities, such as the electron-based microscopy or computational modeling for predictive or correlative analysis.

Major challenges facing society today, such as advancing human health, understanding the food, energy, water nexus and exploring the planet Earth at all scales, require deep understanding of complex and heterogeneous systems. This leads to critical needs to develop multimodal characterization for many scientific fields including energy storage, catalysis, nano- and quantum-materials, environmental science, nuclear energy science, Earth/planetary/space science, semiconductor engineering and biomedical science.

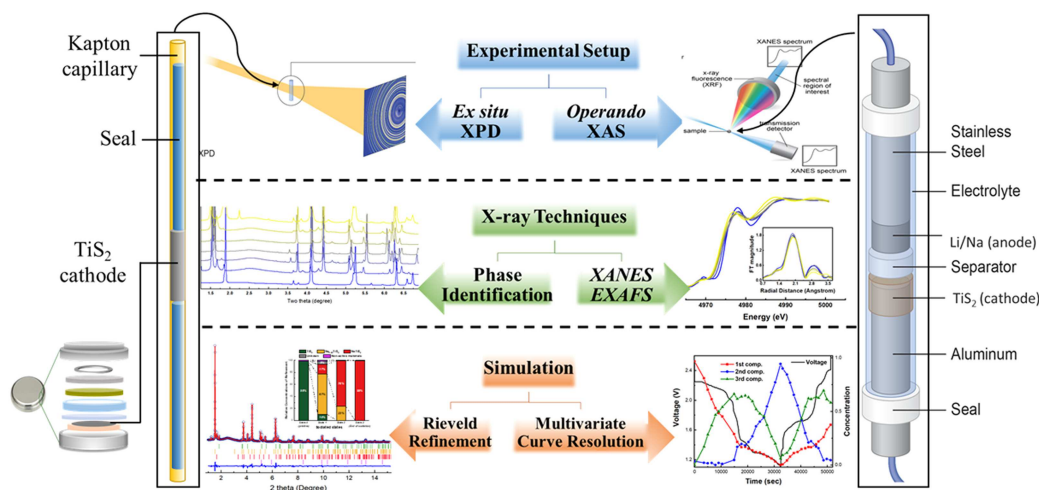


Figure 8. Studying TiS_2 , a cathode material for Li-ion and Na-ion battery using multimodal synchrotron characterization analysis. Figure reproduced [73].

This section will provide a general description of the current state of multimodal approaches at NSLS-II. We then focus on discussing the future trends, emphasizing the challenges and opportunities for synchrotron facilities.

illustrates how with a multimodal synchrotron characterization approach, different beamlines at NSLS-II collectively can provide a comprehensive analysis.

In a sense, multimodal analysis has always been a method of research, with scientists relying on complementary techniques to address a scientific question; however, what is new at a synchrotron is the coordination between different beamlines and techniques requiring more organized architecture at the beamline, both hardware and software, to enable a seamless integration between different techniques.

Many synchrotron beamlines are designed to allow users to carry out multiple techniques and characterization methods in one setup, and hence intrinsically providing multimodal characterization capability. Here we emphasize combining techniques across beamlines and with other experimental and computational techniques, which adds more complexity and yet may enable a greater range of applications and broader impacts.

3.2. Current state-of-the-art for multimodal synchrotron characterization

There are many multimodal analysis activities at NSLS-II and many other synchrotron light sources [83–90]. At NSLS-II, multimodal synchrotron characterization has been applied to enable a range of scientific research. Approximately 30% of NSLS-II users use more than one beamline. Existing examples include: (a) multimodal imaging by combining x-ray microscopy techniques with different length scales or contrast mechanisms [91, 92] or other imaging methods [93, 94], (b) combining x-ray diffraction and spectroscopy with self-consistent theoretical modeling [95, 96], (c) x-ray scattering combined with neutron scattering with a joint model [97, 98], (d) x-ray diffraction combined with density function theory

analysis [99, 100]. Complex and heterogeneous structures are a common theme in these studies.

Energy storage is an inherently complex and often heterogeneous problem; understanding the phase evolution as a function of synthesis parameters and electrochemical cycling conditions is crucial but is often challenging due to such complexity. As such it serves as a good example that can be applied to many other materials science subfields which are concerned with the processing-structure–property-functionality relationship.

Figure 8 illustrates the analysis of the chemical reaction states in a TiS_2 battery electrode in Li-ion and Na-ion batteries by combining *operando* x-ray absorption spectroscopy (XAS) at the inner-shell spectroscopy (ISS) and tender energy x-ray absorption spectroscopy (TES) beamlines with *ex situ* x-ray powder diffraction (XPD) at the x-ray powder diffraction beamline at NSLS-II. Different ranges of x-ray energies were used at the ISS and TES beamlines to access the Ti and S edges of TiS_2 , respectively. In addition to the complementary techniques (diffraction vs spectroscopy) and energy range (hard to tender x-rays), the integration of data analysis between different techniques for multimodal synchrotron characterization is critical. In this example, powder diffraction data analysis was conducted with Rietveld refinement for crystalline phase identification and compared with the modeling of Ti extended x-ray absorption fine-structure spectroscopy. Computational calculation of multivariate curve resolution-alternating least squares was also applied to provide the phase evolution information. Overall the combination of different synchrotron techniques and computational analysis, led to a more detailed understanding of the reaction mechanisms [101].

3.3. Future trends on beamline hardware: cross-beamline experiments

Multimodal experiments are generally categorized into two types in terms of technical needs: (a) static samples: the same

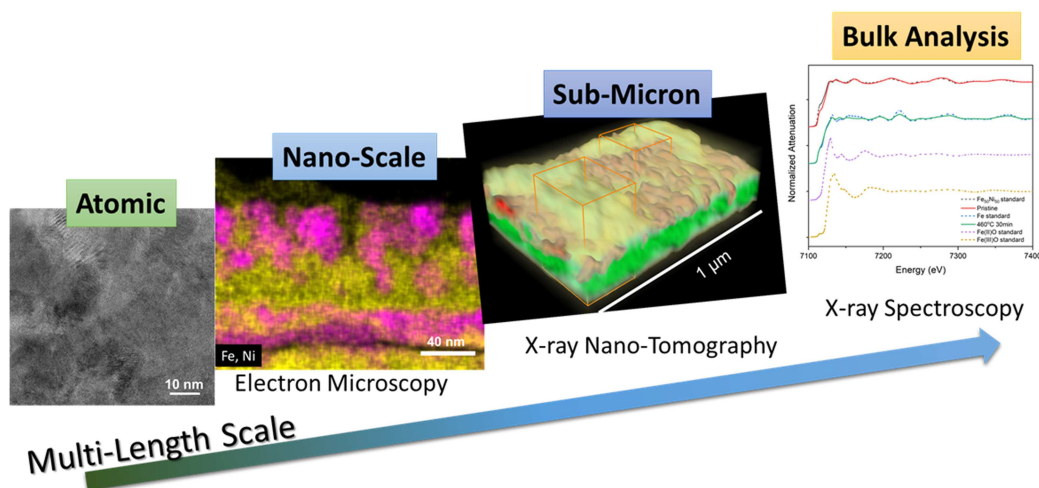


Figure 9. Multi-scale analysis of nano-metallic pattern formation from solid-state interfacial dealloying of a Fe–Ni alloy by Mg in a thin film geometry. TEM, x-ray nano-tomography and XAS analysis were combined across multiple length scales [102].

samples need to be measured across different beamlines without physical changes. This is common for fields such as geology and cultural heritage where each sample is a unique object that cannot be reproduced, but it is applicable for many areas of research. For these types of measurements, simple and fast sample registration between beamlines and laboratory techniques is critical. This leads to the need for developing common fiducial markers, common sample mounts, sample tracking and sample position registration methods. Beam damage may also need to be addressed to ensure samples remain unchanged across beamlines. (b) *Operando in situ* experiments: here the scientific topic requires measuring samples that are evolving under various conditions. In some systems, it may not be feasible to measure the exact same samples across different beamlines because the samples have evolved after one measurement and cannot be reused. To enable such studies consistently across beamlines, *in situ* sample environments need to be compatible across different beamlines in order to create the same *operando* conditions.

Figure 9 shows an example of multimodal analysis conducted on nano-metallic pattern formation via solid-state interfacial dealloying using transmission electron microscopy (TEM) at the Center for Functional Materials (CFM) at BNL, and x-ray nano-tomography with fluorescence and x-ray absorption spectroscopy at the HXN and BMM beamlines at NSLS-II [102]. The interconnected nano-scale features were analyzed with the TEM. However, this provides a limited field of view and has challenges in analyzing 3D morphology. These were resolved at the HXN beamline; the chemical states resulting from dealloying were determined by XAS bulk analysis. The analysis was conducted on individual samples as the sample preparation requirements for the three techniques are different. Methods can be developed to enable robust extraction of sub-volume of interests from a larger sample after x-ray analysis to study them in the TEM. Coordination between instrument at different facilities to enable measurement from the same region at the beamlines

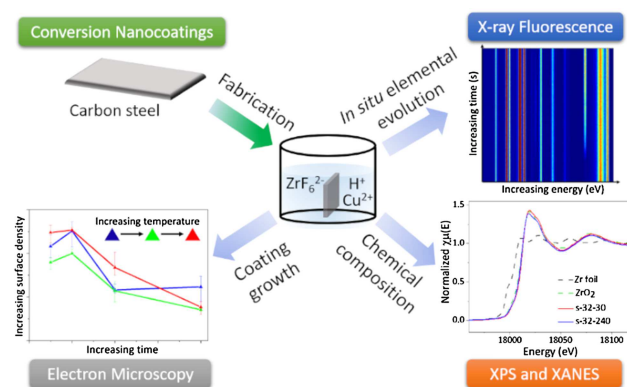


Figure 10. An example of a multimodal industrial study of surface treatment by chemical conversion for protecting materials from corrosion. Complementary techniques were integrated to analyze the chemical conversion process at a synchrotron using *in situ* XRF analysis with a micro-fluidic cell, the chemical products by combined synchrotron XAS and laboratory XPS, and the surface morphology by electron microscopy [103].

and other instrument would further enhance the multimodal analysis.

3.4. Future trends in software: data infrastructure for acquisition, management, analysis and visualization, coupled with theoretical modeling

Data acquisition, management, analysis and visualization play a crucial role in synchrotron x-ray multimodal characterization. The major challenges and opportunities are in two key areas: (1) big data driven by high data acquisition rate and *operando* studies needs to be coordinated and integrated across beamlines or even across facilities, and (2) complex data driven by combining advanced techniques for multimodal analysis with higher dimensions.

First, data acquisition and management—the data acquisition rate at new imaging synchrotron beamlines is truly unprecedented. This is already a pressing issue for individual beamlines; coordinating and integrating data across beamlines

requires a facility-wide coherent infrastructure. NSLS-II is at the forefront of this effort with its development and facility-wide deployment of BlueSky and DataBroker systems, which ensure a consistent data architecture, as well as consistent data acquisition and management across the facility. Further efforts enabling data access across beamlines are critical, and involve IT/data policy and IT infrastructure.

Second, data analysis and visualization. The challenge is to analyze and visualize complex, high dimensional data, and to reduce data from multiple sources into a cohesive, quantitative representation of the system, leading to scientific interpretation. Developing general tools for flexible and modular data comparison, integration and higher dimensional data visualization will bring great impacts. Tools should provide information such as transferable data analysis history and metadata tracking. Open-source software platforms offer great advantages for transparency; the expandability and documentation are crucial to ensure the development effort is sustainable. With the recent advancement in computational modeling methods, theoretical modeling and simulation efforts which allow inputs from, or comparison with, multiple experimental techniques will be an important future direction.

3.5. Future trends in facility operations, a paradigm shift on synchrotron research

There are several facility functions that are crucial to enable effective multimodal research. These include user proposal access and review processes, coordination with user training and providing support laboratories with relevant capabilities to support these activities.

In addition to research by academia, there is a great potential to attract industrial partners, with complex engineering and applied systems problems to solve. An example is a recent study of chemical conversion thin film coatings from Henkel Corp. for protecting steel substrates from corrosion, used mainly for the automobile industry (figure 10); this example highlights the power of multimodal characterization by electromicroscopy, *in situ* x-ray fluorescence (XRF) and XAS at a synchrotron facility, and laboratory x-ray photoelectron spectroscopy (XPS) analysis to provide a complete mechanistic understanding of the chemical evolution of the coatings [103].

It is clear that multimodal characterization will continue to grow due to both the demands from the scientific community, and the rapid technological advances occurring at synchrotron facilities, and will become a near omni-present feature of synchrotron work in the future.

4. Computation and data science

The application of data science to experiments performed at synchrotrons in the past few years has slowly started to alter the way science is performed. In the future, we will move toward embracing more data science methodologies and technologies. This will enable us to perform autonomous experiments, where

data science is tightly integrated in the design and measurement itself, and where near real-time analysis across facilities is common.





Data movement, curation and access will require larger and larger computing resources, and the question of how to access these resources will be front and center of facility operations.

In this section we will discuss the current state of the art automated experiments as employed in the field of structural biology at NSLS-II. The field of machine learning (ML) and artificial intelligence (AI) and how it can be applied to data analysis and experimental steering is an area of particular interest and potential for the future.

4.1. Current state of the art

4.1.1. Automatic experiments for MX. Macromolecular crystallography is the premier technique for elucidating the structure of biological molecules. Modern beamlines are designed to make collection of diffraction data straight forward even when examining the most challenging of samples.

Two state-of-the-art macromolecular crystallography (MX) beamlines at NSLS-II began user operations in 2016. The highly automated (AMX) and frontier (FMX) beamlines are both equipped with six-axis cryogenic sample mounting robots, high capacity cryo-dewars accommodating up to 384 samples in spine standard containers [104], GUI-based data collection software (LSDC), and data processing suite of programs. All diffraction data are written to a centralized computing facility that is capable of providing rapid/instant feedback. Real-time data handling is supported by a fast network (56 Gb s⁻¹ Infiniband), a dedicated computing cluster of about 750 cores, a GPFS fast buffer (one fast 20 TB SSD array per beamline) and GPFS medium term storage (currently 800 TB of data). With these facilities and the beamlines characteristics ($7 \times 5 \mu\text{m}^2$ and 4×10^{12} ph/s for AMX and $1.5 \times 1 \mu\text{m}^2$ and 3×10^{12} ph/s for FMX) it is possible to rapidly interrogate crystal samples from the most challenging projects. AMX and FMX routinely generate usable data from difficult samples such as micron sized crystals embedded in opaque media and poorly diffracting crystals of large assemblies. AMX and FMX feature a growing suite of protocols for automated data collection from all but the most difficult specimens.

Conventional diffraction from large single crystals (50 μm or larger) is the most straightforward experiment to automate. A typical use case for automated large single crystal MX is ligand and binding studies on well characterized crystals. The ligand binding use case drove development of the first 'single crystal' automation protocol at AMX/FMX: optical loop centering  coarse x-ray area centering  fine x-ray area centering  fine x-ray line centering at 90°  user defined data collection [105]. In this protocol, the sample is centered at the location with the highest number of Bragg spots, and a dataset is collected using predetermined parameters. Currently this protocol delivers diffraction datasets from approximately 22 samples

per hour. Using only loop centering increases throughput to 40 samples per hour. All x-ray operations (data collection and x-ray crystal centering) can be performed within the envelope of an accurate radiation damage budget.

The development of a second automation protocol, ‘raster screening’, was driven largely by users who want to verify diffraction as part of their crystallization efforts. Subsequently a second important use case for the same protocol arose: serial crystallography from mesh-mounted crystals. The workflow for ‘raster screening’ is very simple (optical loop centering followed by x-ray screening of the area with user defined granularity). Depending on the sample mount, the raster step size and area, and the desired exposure time, the typical throughput for this protocol varies from 5 samples per hour (for large rasters on serial crystallography samples) to 30 samples per hour (for screening crystallization or cryo samples).

Many mature facilities have optimized one or more automated data collection protocols with enhanced capabilities such as identifying best diffracting volumes or data collection along linear trajectories [106, 107]. At the European synchrotron ESRF MASSIF-1, dedicated to automated diffraction from crystals larger than 50 μm , the six-axis robotic sample changer doubles as a sample goniometer capable of supporting a variety of automated workflows, with a yearly throughput of 15 000 samples [108].

At NSLS-II, we believe that the success of future automation will depend on smart protocols that can determine optimal data collection trajectories based on the number of useful Bragg spots. By including only indexable spots in the overall count, smart trajectories would avoid high count/low quality diffracting volumes that contain split spots, multiple lattices, or background artifacts such as salt lines. This will allow the protocol to define trajectories through optimal diffracting volumes, to generate optimal data using automatic data collection. Diffraction from multiple-crystals can also be optimized using a smart protocol, which will terminate data collection when a desired completeness is achieved, or alternatively will use redundancy to improve signal to noise until experimental phasing succeeds.

European facilities currently provide real time tracking of data collection and data processing using *ISPyB* [109]. At NSLS-II we have adopted *ISPyB/SynchWeb* as a working model for tracking progress of data collection and processing [110].

4.2. Future trends

4.2.1. Machine learning for data analysis. Synchrotron facilities today provide extremely high data collection rates. There is a corresponding challenge with respect to data analysis, since conventional manual data analysis does not scale to these rates. Automated data analysis workflows are increasingly necessary; yet these often omit the qualitative judgments that human experimenters make as they explore, triage and classify datasets. In this regard, modern ML methods are extremely attractive, since they offer the opportunity to generate automated analysis workflows that capture some aspects of human heuristics.

Ongoing work at Brookhaven National Laboratory (BNL) has been leveraging modern advances in machine-learning to automate the analysis of x-ray scattering data [111–117]. Modern deep learning methods were found to be especially effective. Deep (multi-layered) convolutional neural networks (CNNs) have emerged as a powerful method for analyzing complex real-world data, including photographs, video, and sound. The multiple layers allow the system to learn a hierarchical internal representation of a given problem space. For instance, in image analysis lower layers of the network respond to basic visual features such as edges, while intermediate layers respond to composite features (particular arrangements of shapes), and final layers can thereby respond to complex aggregate concepts (such as ‘person’ or ‘car’). Since x-ray area detector data is conceptually similar to a photograph (two-dimensional array), it is natural to exploit existing CNN architectures to classify x-ray scattering data.

Research at BNL exploited deep-learning CNNs to classify x-ray scattering images in a variety of ways (testing >100 distinct tags), including identifying experimental errors (blocked beam, parasitic scattering streaks), image features (peaks, rings, etc) and specific materials. The research both confirmed that CNNs can achieve high performance on these kinds of tasks, while also highlighting a set of challenges. First, it is interesting to note that x-ray scattering data is inherently delocalized: since it is roughly a Fourier transform of the material structure, features across the entire image can be relevant for a given recognition problem. By comparison CNNs are designed to respond and aggregate local image features. Nevertheless, when correctly trained, a CNN can identify features relevant in an x-ray scattering image (such as peaks and rings) in much the same way a trained expert does. Second, a key challenge in the use of ML methods is acquiring a training dataset. While experimentalists have access to large datasets, these data are typically not tagged appropriately and thus not suitable for supervised ML methods. To overcome this challenge, one can simulate highly realistic data. For x-ray scattering, the underlying mechanism of the pattern formation, as well as the sources of noise and artifacts, are well understood. Synthetic data can then be used for training a CNN, after which a short retraining phase on a small set of tagged experimental data closes the gap between synthetic data and experimental reality [115, 118]. Finally, x-ray scattering involves a range of image defects due to experimental geometry (e.g. refraction distortion) or detector (e.g. intermodule gaps in images). These defects can be handled by using healing algorithms as a pre-processor [119, 120], which thereby prevents the deep learning method from focusing on highly-evident but ultimately irrelevant image features.

4.2.2. Autonomous experiments. A key challenge facing synchrotron facilities is to maximize not just the data collection rate, but also the *value* of each datum. Continual advances in hardware and software have enabled tremendous increases in the data collection rate. However, if this boost in data throughput is not accompanied by a corresponding increase in *useful* data, its impact on accelerating scientific discovery will remain marginal. The data spaces probed

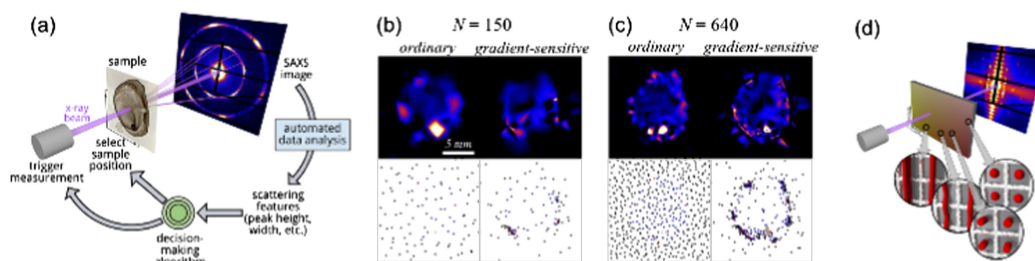


Figure 11. (a) A schematic illustrating autonomous scanning-probe SAXS imaging experiments on a pattern formed by solution-cast nanoparticles, performed at the CMS beamline at NSLS-II [63, 125]. (b) and (c) Comparison of two autonomous data collection strategies, one based on ‘ordinary’ Gaussian process regression (left panels) and the other on a ‘gradient-sensitive’ variant (right panels), with each after (b) 150 and (c) 640 measured data points. The gradient-sensitive algorithm makes decision using uncertainties weighted by local gradients in the surrogate model. (d) A schematic illustrating scanning-probe SAXS experiments on a combinatorial sample library, in which material parameters vary across the sample surface.

in modern synchrotron experiments are highly heterogeneous. Data may span real space (e.g., scanning-probe images of multi-component materials), or experimental parameter spaces (e.g., nanoscale structure measured as a function of temperature and composition). As the data space of interest expands in size, dimensionality, and complexity, traditional experimental strategies based on intuition or exhaustive exploration become increasingly inefficient and wasteful. In order to probe complex data spaces efficiently, intelligent experimental guidance methods—wherein the information content of a measured data-point is maximized—are just as important as throughput. Such methods will be especially critical in enabling experiments with limited budget for time (e.g., rapid-access beamtime) or x-ray dosage (e.g., radiation-sensitive materials).

Machine-guided autonomous experimentation is a promising strategy to maximize the value of each measurement. Automation increases data collection rate, while carefully designed algorithms can lead to selection of *optimal* follow-up experiments based on the data collected so far. One common approach to autonomous experimentation is to closely integrate a particular physical theory into the experimental control algorithm. This ‘physics-informed’ approach leverages known physics and has been used in recent successful implementations of machine-assisted experimental guidance [121–124]. For example, a recent study that involved synchrotron x-ray diffraction (XRD) experiments on metallic alloy systems [121] combined existing structural database and physical–chemical theories with newly performed XRD experiments on combinatorial sample libraries, in order to train and iteratively retrain a ML model for glass-forming regions in ternary composition space. This study, in which the model was used to both improve theoretical parameters and provide a basis for selecting combinatorial libraries to be prepared and measured in the next iteration, led to discovery of new metallic glasses [121]. There are, however, inescapable trade-offs associated with this approach. First, by design, the applicability of this approach is limited to those materials systems or physical phenomena for which a great deal of knowledge already exists. Second, reconfiguring the workflow to handle a new class of materials involves considerable work to select and integrate a new theory. Finally, when the decision-making algorithm is closely

coupled to a specific class of materials, the workflow is of course not generally applicable.

An alternative, complementary approach is ‘physics-agnostic’ methods of autonomous experimentation that are being developed by a collaboration between the DOE Center for Advanced Mathematics for Energy Research Applications (CAMERA), BNL’s Center for Functional Nanomaterials (CFN), Computational Science Initiative (CSI), and NSLS-II. This effort recently led to successful implementation of autonomous experiments at the complex materials scattering (CMS) beamline at NSLS-II, where a general machine-guided algorithm was used to control a variety of x-ray scattering experiments.

In a set of proof-of-principle studies, autonomous scanning-probe SAXS was used to efficiently map heterogeneous patterns in real space [63, 125]. The experiments performed are based on a workflow pipeline consisting of: automated sample handling and data acquisition; real-time data processing; and decision-making algorithms, which close the autonomous feedback loop (figure 11(a)). These algorithms, based on Gaussian process regression, take processed data as input, provide a ‘surrogate’ model by interpolating existing data, and select the unmeasured point in the data space with highest uncertainty in the model as the next experimental point to be measured, thus maximizing the information gain per measurement. The results demonstrate that this method efficiently maps the entirety of a parameter space, with resolution improving as it collects additional data (figures 11(b) and (c)). Since this proof-of-principle experiment, the autonomous x-ray scattering pipeline at the CMS beamline has been successfully applied to a wide range of material problems, including parameter space exploration based on combinatorial sample libraries (figure 11(d)) and lithographic sample arrays. A robotic sample exchanger was used where appropriate to further expand the size of parameter space that can be explored in a given experiment.

A key feature of the above decision-making algorithms [125] is that they are independent of the nature of experimental techniques used and are applicable to any types of data space in which quantities based on processed data (fluorescence or scattering intensity, degree or orientation of anisotropy, grain

size, crystal structure, etc) depend on automated experimental control parameters (spatial coordinates, temperature, pressure, composition, etc). As such, the software codes, software infrastructure and best-practices are all directly transferable, with minimal customizations, to other beamlines at NSLS-II and elsewhere. The corresponding trade-off is that this method does not inherently leverage known materials physics to constrain and optimize the search process.

Autonomous experimentation at synchrotron facilities is still in its infancy and requires an enormous amount of further development to realize its potential to substantially expand the scope of user science. Here we note two future development directions that we believe are important. One is the integration of automated material synthesis and processing capabilities, such that autonomous decision-making algorithms guide not only the material characterization via x-ray and other ancillary methods but also the on-the-fly generation of high-value samples to be studied at the beamline. Such capabilities could revolutionize the role of synchrotron experiments in materials discovery, by enabling intelligent exploration of the vast, multi-dimensional material and processing parameter spaces associated with modern functional materials.

The second direction is to develop methods to incorporate varying degrees of existing physical knowledge into the autonomous decision-making process, to further enhance its ability to guide experiments, while not sacrificing the generality of the decision-making platform. The physics-agnostic approach described above completely ignores existing knowledge about the material system or phenomenon under study. One difficulty is that depending on the given study, the nature of physical knowledge that could guide the experiment can range from being highly qualitative, or even intuitive, to highly quantitative, based firmly on a well-developed theory and/or on extensive simulation results. A key observation here is that even qualitative knowledge can be effective in guiding an experiment. Thus, development of general autonomous decision-making methods or protocols that can exploit a varying depth of physical knowledge would likely benefit a broad range of synchrotron users who study new materials or complex phenomena.

4.2.3. Remote data analysis workflows and use of distributed resources. The data volume and velocity produced by modern synchrotron beamlines is going up at an ever-increasing rate. This results in either a higher throughput of experiments or the collection of larger and more complex datasets. For both of these cases, the role of remote data analysis workflows plays an important role.

As experiments become shorter, the amount of beamtime required for a particular measurement will reach a limit where it is no longer worthwhile for a user to physically visit the synchrotron. For this case, remote data analysis and data pipelines will play a crucial role in steering the experiment from a remote institution and in performing an optimal experiment.

Keeping pace with the challenge of more complex and larger data requires the use of larger and larger computational resources. It is likely that it will not be feasible for a single facility to provide all the computational resources required.

This will lead to having to deal with a heterogeneous set of infrastructures and the challenges of co-scheduling experimental and computational resources.

Further, for these large data volumes, users will not always have the resources to perform analysis at their home institution and will need to rely on tools such as Jupyter providing them remote access to analysis resources in a transparent way [71]. In addition, with the growth of the multimodal approach, it seems likely that users will need to combine data taken at different facilities, this too will present its own unique set of challenges.

5. Technology

5.1. Optics

With the advance of ultimate source properties of the new generation light sources, the quality of the focusing devices used has been drastically improved over the past decades. The new aberration-free x-ray wavefront sources require high precision and low aberration optics to transfer this source quality to the sample. Technologies used in the fabrication of x-ray optics include lithographic nanofabrication for diffractive [126] and refractive lenses [127], surface figuring with atomic precision for total reflection and multilayer mirrors [128–130] and thin-film technologies for multilayer lenses [131–136]. We are now able to achieve small focuses of 10 nm or less by using state-of-the-art Fresnel zone plates, multilayer mirrors in Kirkpatrick–Baez geometry, and multilayer Laue lenses.

Optical elements must be manufactured to very high tolerances, and most importantly maintain their outstanding characteristics under their complex operational conditions in the beamlines.

X-ray wavefront preserving or x-ray diffraction limited mirrors (with typically 1 nm RMS figure error, sub 100 nrad RMS residual slope error) are required. In turn this requires methods to measure the characteristics of optical elements, such as the figure error and roughness of mirrors, the groove density distribution of diffraction gratings, or the phase coherence of diffractive optics as well as methods for optimally aligning and tuning optics *ex situ* and *in situ*, at the beamline.

The application of different instruments available in an optical metrology laboratory addresses different potential sources of error affecting beamline performances. *Ex situ* metrology allows one to address most of the problems before the installation of the optic at a beamline, provide feedback on design and guidelines and ensure vendor compliance [137–139]. This requires a very good synergy between optical metrology and optical simulation [140, 141].

Ex situ optimization of a complex optical set up prior to beamline installation can also accelerate x-ray commissioning time. Due to the continuous improvements in the quality of optical surfaces, the new challenge for x-ray optics is minimizing additional slope/height errors introduced by mounting the substrate into its holder and adding a complex cooling mechanism. For active optics, optical metrology allows one to minimize or cancel parasitic distortions (including bend hysteresis,

roll errors and sagittal bending or twisting) induced during the mounting [142].

In parallel, the development of *in situ* at-wavelength metrology tools (i.e. metrology using the x-ray beam itself) for x-ray component characterization, alignment and beamline performance studies is a necessary complementary method of visible light metrology. The ultimate performance of the optics is often affected by the factors such as x-ray beam alignment, mechanical and thermal drifts, and vibrations. The best way to overcome these limitations and to improve the performance of x-ray optics is using at-wavelength and *in situ* techniques. Several at-wavelength metrology techniques including Hartmann x-ray wavefront sensors, grating interferometry, Fresnel propagation iterative algorithms, and ptychography have been developed over the last two decades [133,143–152].

5.2. Detectors

5.2.1. Pixel size. Current microelectronics technology allows visible light detectors to have pixels in the single-micron range. However, there are several issues which limit the application of these technologies to x-rays. For soft x-rays, the range of absorption depths is a few microns, and the range of the generated electron–hole pairs is similar. The active depth of the sensor need only be a few microns, so lateral diffusion during charge drift is not an issue. For hard x-rays this is not the case. For silicon, sensor thicknesses must be several hundred microns if a reasonable detection efficiency is to be maintained. This results in significant lateral diffusion of charges as they drift through this thickness, resulting in a minimum effective resolution of order 20 μm . For photon-counting detectors, it is possible to use this diffusion, and the resulting signal distribution among neighboring pixels, to interpolate the photon absorption site with sub-pixel resolution. This has been demonstrated, using frame-oriented detectors, but the requirement to read out a full frame in order to analyze each photon and to prevent overlapping events results in a significant rate limit. Photon-by-photon processing on-chip would potentially remove those limitations. This would require significant on-pixel electronics and has not yet been achieved. This requirement also competes with the pixel size, since electronics requires real-estate on the detector.

5.2.2. Frame rate. The limit on frame rate is more driven by computing capabilities than by detector technologies. Current detectors already have outstripped the ability of data storage systems to handle the data rate. The rate capability of a detector can usually be enhanced by simply increasing the parallelization of the readout system, i.e. by increasing the number of output ports on the device, with some power-rate trade-offs. Ultimately, every pixel could be read out independently. The ability of computers to swallow such huge data rates is not so easy to enhance. For relatively short bursts, data can be cached on-detector, but the amount of local memory available is also finite. Eventually, we will have to abandon the idea of storing all of the raw data, and only storing reduced or processed data. ML/AI can help to achieve this goal. This path forward will

rely on exquisite calibration of the detector. The sample itself will become the raw data repository.

5.2.3. Energy and time resolution. The best energy resolution x-ray detectors at this time are those based on cryogenics, the microcalorimetric transition edge sensors, and those based on Cooper pair production, the Josephson junction devices. These are beginning to be sufficiently developed to be accessible to non-expert users, but still have disadvantages such as limited rate capability and complex and bulky operating hardware.

For time resolutions below 1 ns, the avalanche photodiode is the leader, although there is much interest in a related device, the low gain avalanche detector. The latter lends itself better to large arrays than the conventional APD, but so far does not have better performance. Much progress has also been made in the development of single photon avalanche detectors (SPADs), which operate in Geiger mode. There is a lot of interest in the medical community in achieving time resolution below 10 ps, primarily from PET developers, since that would bring the spatial resolution of such an instrument below 1 mm.

5.2.4. Smart detectors. As discussed above, the field needs to find ways of at least partially analyzing our data on-detector, if not on-chip, if our computer systems are to cope. On-chip electronics raises the issue of pixel size, and so it will probably be necessary to move to so-called 3D integration, which extends the integrated structure by stacking chips atop each other. Each added layer provides real-estate for electronic circuitry. Two-layer x-ray detector systems have been built, but it should be possible to add more layers; industry foundries have memory systems with many layers as a way to move beyond Moore's law. All of this circuitry consumes power, and so we will have to develop more effective cooling systems for these advanced detectors, such as silicon micro-channels to carry coolant to within a few microns of the circuitry. Such a highly integrated system will likely preclude the storage of raw data.

5.2.5. High energies. Efficient detection of very hard x-rays (>20 keV or so) requires a high atomic number (Z) sensor so that the x-rays are efficiently absorbed. There are semiconductors which have high Z , such as germanium, selenium and the II–VI compounds such as cadmium telluride, cadmium zinc telluride or gallium arsenide. Of these, the highest quality crystals are those of germanium, while selenium is only available in the amorphous state. The II–VI compounds are difficult to grow in large volumes without incurring high defect densities. Cadmium telluride provides the best quality crystals, but detectors made from that material have some disadvantages, such as time-dependent efficiency (i.e. polarization). Germanium is a much better material but has the disadvantage of requiring cryogenic cooling to remove thermally-generated carriers. However, it does offer the best energy resolution of all the high- Z materials due to the absence of traps and defects. The effort of cryogenic cooling is much reduced by using modern closed-cycle cryostats, which are compact and quiet.

5.3. Insertion devices

Progress in insertion devices (IDs) have had a major impact on the performance of synchrotron radiation facilities following the invention of the permanent magnet (PM) structure by Halbach [153], the development of the in-vacuum undulator (IVU) [154], its mini-gap device [155] and the invention of various PM based elliptically polarizing undulators (EPU)s.

The first utilization of a superconducting undulator (SCU) was at Orsay in the 1970s. Though it is only recently that SCUs have become competitive with IVUs. The cryo-permanent magnet undulator (CPMU) concept was developed to further improve the performance of PM based IDs [156]. Another extension of PM technology is the segmented adaptable gap undulator (SAGU) [157].

With the deployment of on-axis injection schemes for new storage rings [158], the requirement of horizontal aperture size and good field region has been greatly reduced to permit the design of IDs formerly possible only for linac based light sources.

In this subsection, the future trends for two types of IDs: PM based IDs and SC based magnets are discussed.

5.3.1. PM based IDs.

5.3.1.1. Cryo-cooled permanent magnet undulators. The current state-of-the-art PM technology for short period planar undulator is the CPMU. The original approach assumed the use of NdFeB magnets which tended to suffer from spin-reorientation transition at low temperatures [159]. Now the majority of CPMUs utilize PrFeB magnets [160] which exhibit no such transitions even at liquid nitrogen temperatures and lower. While a room-temperature IVU can be longer than 5 m, the longest CPMU so far is 2.0 m due to engineering challenges caused by large contraction of the magnet arrays due to temperature change.

Due to the strong dependence of gap on the transverse resistive wall impedance [161], it may not be practical to reduce the gap of an IVU to lower than 4 mm in a storage ring. CPMU devices can achieve the same level of field with a larger magnetic gap, which will be of more importance in future accelerators requiring higher beam stability.

5.3.1.2. Segmented adaptive gap undulators. The original idea of giving adaptive gap profile to the magnetic arrays in ID was the proposed ‘Constant Resonant Energy Undulator’ [162]. The idea was that the period/gap combination of magnetic arrays follow the profile of the electron beam envelope. In reality it is not practical to use magnets of different sizes to create such an array. Therefore, the concept of SAGU was proposed.

In an SAGU, the period length is the same in one segment but varies with the longitudinal location. The gap is the smallest in the area where the vertical beta function of the electron beam is the smallest. With this scheme more photons can be generated from the same straight section than from a conventional device. This concept can be expanded to cryo temperature devices or even to superconducting devices. There are some technical issues such as expandable continuity sheets

and in-vacuum correction coils in the seams which must be solved.

5.3.1.3. Elliptically polarized undulators. The advanced planar polarized light emitter (APPLE) type undulator [163] and its improved version, the APPLE-II, have been the main workhorse for PM based EPU)s for many years because of its simple magnetic structures and its ability to produce all possible polarization combinations. Detrimental non-linear effects from the generated field have been dealt with by the implementation of a current-strip scheme [164].

With the utilization of on-axis injection in the future storage rings, more restrictive but more effective magnetic structure such as the DELTA [165] or APPLE-X [166] can be used. The only disadvantage for these devices is the inability to measure the devices from the side of the arrays. Therefore, they require a dedicated magnetic measurement facility.

5.3.2. Superconducting-based magnets.

5.3.2.1. SCU/SCW. The first SCU employed in a light source ring was in 1979 at LURE in Orsay. While SC wigglers are used in many places for the generation of high energy photons, the use of SCUs with small periods has not been widespread due to technical difficulties. Substantial R & D efforts by the groups at Karlsruhe and Argonne National Lab have now started coming to fruition [167, 168]. While an SCU has the inherent advantage of not suffering from radiation demagnetization, SCUs which to date are NbTi based, have comparable performance with PrFeB based CPMU [169] and also have hysteresis issues inherent to iron based magnets. However, once Nb₃Sn-based devices with reasonable RMS phase errors are built, the SCU is likely to have a clear performance advantage over PM based devices.

SCWs have been utilized at many places for the generation of high energy photons from relatively lower energy electron beams. Three pole SCW of 10 T and multipole wigglers of 4.5 T have been fabricated. Use of Nb₃Sn and high-temperature SC tape/wire is anticipated to improve the performance of SCW in the future.

5.3.2.2. Superbend. Another SC based photon source which is not an insertion device is so-called the ‘superbend’ [170]. It remains to be seen if the future design of ultra low emittance rings can accommodate superbends in their lattice design.

6. Conclusion

In this article, we have described current and future trends in synchrotron science, illustrating them with examples from the NSLS-II at Brookhaven. We should be clear that this is a snapshot of activities at NSLS-II and is not meant to be a review of similar activities elsewhere. The field is highly dynamic presently, driven by advances in sources, optics, detectors and data science. Extremely difficult or impossible experiments from a few years ago have been transformed into routine measurements that take a few minutes. This is driving an explosion of high impact science that seems unlikely to slow any time soon. It is a very exciting time in the field. In regard

to Roger Cowley, to whom this issue is dedicated, it is clear he would be energized by these results and certainly would be exploiting them to address some of the most important questions of our time in his chosen field of condensed matter physics.

Acknowledgments

The authors would collectively like to acknowledge their colleagues and collaborators who contributed so much to the work that is reflected in this article and deeply regret the space requirements that prevented their individual acknowledgment.

This research used AMX, BMM, CHX, CMS, FMX, FXI, HXN, ISS, SIX, SRX, TES, and XPD of the National Synchrotron Light Source II and Center for Functional Nanomaterials which are U.S. DOE Office of Science Facilities at Brookhaven National Laboratory under Contract No. DE-SC0012704.

The Life Science Biomedical Technology Research resource is primarily supported by the National Institute of Health, National Institute of General Medical Sciences (NIGMS) through a Biomedical Technology Research Resource P41 Grant (P41GM111244), and by the DOE Office of Biological and Environmental Research (KP1605010).

ORCID iDs

Stuart Campbell  <https://orcid.org/0000-0001-7079-0878>

Kevin G Yager  <https://orcid.org/0000-0001-7745-2513>

References

- [1] Yan H, Bouet N, Zhou J, Huang X, Nazaretski E, Xu W, Cocco A P, Chiu W K S, Brinkman K S and Chu Y S 2018 Multimodal hard x-ray imaging with resolution approaching 10 nm for studies in material sciences *Nano Futures* **2** 011001
- [2] Ulvestad A *et al* 2019 Multimodal x-ray imaging of grain-level properties and performance in a polycrystalline solar cell *J. Synch. Radiat.* **26** 1316–21
- [3] Da Silva J C, Pacureanu A, Yang Y, Bohic S, Morawe C, Barrett R and Cloetens P 2017 Efficient concentration of high-energy x-rays for diffraction-limit imaging resolution *Optica* **4** 492–5
- [4] Somogyi A, Medjoubi K, Gil B, Le Roux V, Ribbens M, Polack F, Philippot P and Samama J-P Optical design and multi-length-scale scanning spectro-microscopy possibilities at the Nanoscopium beamline of Synchrotron Soleil. *J. Synch. Radiat.* **22** 1118–29
- [5] Grew K N, Chu Y S, Yi J, Peracchio A A, Hwu Y, De Carlo F and Chiu W K S 2010 Nondestructive 3D elemental mapping and analysis of solid oxide fuel cell anode *J. Electrochem. Soc.* **157** B783–92
- [6] Nelson G J, Harris W M, Izzo J R Jr, Grew K N, Chiu W K S, Chu Y S, Yi J, Andrews J C, Liu Y and Pianetta P 2011 Three dimensional mapping of nickel oxidation states using full field x-ray absorption near edge structure nanotomography *Appl. Phys. Lett.* **98** 173109
- [7] Meirer F, Cabana J, Liu Y, Mehta A, Andrews J C and Pianetta P 2011 Three-dimensional imaging of chemical phase transformations at the nanoscale with full-field transmission x-ray microscopy *J. Synch. Radiat.* **18** 773–81
- [8] Chen Y-T, Chen T-Y, Yi J, Chu Y S, Lee W-K, Wang C-L, Kempson I M, Hwu Y, Gajdosik V and Margaritondo G 2011 Hard x-ray Zernike microscopy reaches 30 nm resolution *Opt. Lett.* **36** 1269–71
- [9] Yang Y, Cheng Y, Heine R and Baumbach T 2016 Contrast transfer functions for Zernike phase contrast in full-field transmission hard x-ray microscopy *Opt. Express* **24** 6063–70
- [10] Miao J, Charalambous P, Kirz J and Sayre D 1999 *Nature* **400** 342
- [11] Fienup J 1982 *Appl. Opt.* **21** 2758–69
- [12] Williams G J, Quiney H M, Peele A G and Nugent K A 2010 *New J. Phys.* **12** 035020
- [13] Kim C, Kim Y, Kim S S, Kang H C, McNulty I and Noh D Y 2014 *Opt. Express* **22** 5528
- [14] Thibault P, Dierolf M, Menzel A, Bunk O, David C and Pfeiffer F 2008 *Science* **321** 379
- [15] Vine D J, Williams G J, Abbey B, Pfeifer M A, Cark J N, de Jonge M D, McNulty I, Peele A G and Nugent K A 2009 *Phys. Rev. A* **80** 063823
- [16] Howells M R *et al* 2009 *J. Electron Spectrosc. Relat. Phenom.* **170** 4
- [17] Robinson I K, Vartanyants I A, Williams G J, Pfeifer M A and Pitney J A 2001 *Phys. Rev. Lett.* **87** 195505
- [18] Williams G J, Pfeifer M A, Vartanyants I A and Robinson I K 2003 *Phys. Rev. Lett.* **90** 175501
- [19] Williams G J, Quiney H M, Dhal B B, Tran C Q, Nugent K A, Peele A G, Paterson D and de Jonge M D 2006 *Phys. Rev. Lett.* **97** 025506
- [20] Abbey B *et al* 2011 *Nat. Photon.* **5** 420
- [21] Nazaretski E *et al* 2015 Pushing the limits: an instrument for hard x-ray imaging below 20 nm *J. Synchrotron Radiat.* **22** 336
- [22] Yan H, Chu Y S, Maser J, Nazaretski E, Kim J, Kang H C, Lombardo J J and Chiu W K S 2013 Quantitative x-ray phase imaging at the nanoscale by multilayer Laue lenses *Sci. Rep.* **3** 1307
- [23] Pelz P M, Guizar-Sicairos M, Thibault P, Johnson I, Holler M and Menzel A 2014 On-the-fly scans for x-ray ptychography *Appl. Phys. Lett.* **105** 251102
- [24] Deng J, Nashed Y S G, Chen S, Phillips N W, Peterka T, Ross R, Vogt S, Jacobsen C and Vine D J 2015 Continuous motion scan ptychography: characterization for increased speed in coherent x-ray imaging *Opt. Express* **23** 5438–51
- [25] Huang X, Lauer K, Clark J N, Xu W, Nazaretski E, Harder R, Robinson I K and Chu Y S 2015 Fly-scan ptychography *Sci. Rep.* **5** 9074
- [26] Huang X, Yan H, Ge M, Öztürk H, Nazaretski E, Robinson I K and Chu Y S 2017 Artifact mitigation of ptychography integrated with on-the-fly scanning probe microscopy *Appl. Phys. Lett.* **111** 023103
- [27] Lin Y, Fang S, Dong S, Kyle S B and Chen F 2015 Enhancing grain boundary ionic conductivity in mixed ionic-electronic conductors *Nat. Commun.* **6** 6824
- [28] Hill M O *et al* 2018 Measuring three-dimensional strain and structural defects in a single InGaAs nanowire using coherent x-ray multi-angle Bragg projection ptychography *Nano Lett.* **18** 811–9
- [29] Lee W-K, Reininger R, Loo W, Gambella R, O'Hara S, Chu Y S, Zhong Z and Wang J 2016 FXI: a full-field imaging beamline at NSLS-II *Proc. SPIE* **9592** 959209
- [30] Ge M, Coburn D S, Nazaretski E, Xu W, Gofron K, Xu H, Yin Z and Lee W-K 2018 One-minute nano-tomography using hard x-ray full-field transmission microscope *Appl. Phys. Lett.* **113** 083109

- [31] Yang H *et al* 2019 Simultaneously dual modification of Ni-rich layered oxide cathode for high-energy lithium-ion batteries *Adv. Funct. Mater.* **29** 1808825
- [32] Sutton M *et al* 1991 Observation of speckle by diffraction with coherent x-rays *Nature* **352** 608–10
- [33] Madsen A, Fluerasu A and Ruta B 2018 Structural dynamics of materials probed by x-ray photon correlation spectroscopy *Synchrotron Light Sources and Free-Electron Lasers: Accelerator Physics, Instrumentation and Science Applications* ed E Jaeschke *et al* (Cham: Springer International Publishing) pp 1–30
- [34] Nogales A and Fluerasu A 2016 X-ray photon correlation spectroscopy for the study of polymer dynamics *Eur. Polym. J.* **81** 494–504
- [35] Brauer S *et al* 1995 X-ray intensity fluctuation spectroscopy observations of critical dynamics in Fe₃Al *Phys. Rev. Lett.* **74** 2010–3
- [36] Dierker S B *et al* 1995 X-ray photon correlation spectroscopy study of Brownian motion of gold colloids in glycerol *Phys. Rev. Lett.* **75** 449–52
- [37] Zhang Q *et al* 2018 Sub-microsecond-resolved multi-speckle x-ray photon correlation spectroscopy with a pixel array detector *J. Synchrotron Radiat.* **25** 1408–16
- [38] Rumaiz A K *et al* 2016 First experimental feasibility study of VIPIC: a custom-made detector for x-ray speckle measurements *J. Synchrotron Radiat.* **23** 404–9
- [39] Ramirez J, Dursch T J and Olsen B D 2018 A molecular explanation for anomalous diffusion in supramolecular polymer networks *Macromolecules* **51** 2517–25
- [40] Lumma D *et al* 2000 Area detector based photon correlation in the regime of short data batches: data reduction for dynamic x-ray scattering *Rev. Sci. Instrum.* **71** 3274–89
- [41] Ponchut C *et al* 2011 MAXIPIX, a fast readout photon-counting x-ray area detector for synchrotron applications *J. Instrum.* **6** C01069
- [42] Radicci V *et al* 2012 EIGAB - EIGER is the next generation of single photon counting pixel detector for synchrotron radiation designed by the PSI-SLS detector group *J. Instrum.* **7** C02019
- [43] Sutton M *et al* 2003 Using coherence to measure two-time correlation functions *Opt. Express* **11** 2268–77
- [44] Falus P, Borthwick M A and Mochrie S G J 2005 Fluctuation dynamics of block copolymer vesicles *Phys. Rev. Lett.* **94** 016105
- [45] Banchio A J *et al* 2006 Many-body hydrodynamic interactions in charge-stabilized suspensions *Phys. Rev. Lett.* **96** 138303
- [46] Kwaśniewski P, Fluerasu A and Madsen A 2014 Anomalous dynamics at the hard-sphere glass transition *Soft Matter* **10** 8698–704
- [47] Angelini R *et al* 2013 Dichotomic aging behaviour in a colloidal glass *Soft Matter* **9** 10955–9
- [48] Guo H *et al* 2010 Connecting nanoscale motion and rheology of gel-forming colloidal suspensions *Phys. Rev. E* **81** 050401
- [49] Fluerasu A *et al* 2007 Slow dynamics and aging in colloidal gels studied by x-ray photon correlation spectroscopy *Phys. Rev. E* **76** 010401
- [50] Fluerasu A *et al* 2010 Dynamics and rheology under continuous shear flow studied by x-ray photon correlation spectroscopy *New J. Phys.* **12** 035023
- [51] Burghardt W R *et al* 2012 X-ray photon correlation spectroscopy during homogenous shear flow *Phys. Rev. E* **85** 021402
- [52] Rogers M C *et al* 2014 Echoes in x-ray speckles track nanometer-scale plastic events in colloidal gels under shear *Phys. Rev. E* **90** 062310
- [53] Kim H *et al* 2003 Surface dynamics of polymer films *Phys. Rev. Lett.* **90** 068302
- [54] Hu X *et al* 2006 Observation of a low-viscosity interface between immiscible polymer layers *Phys. Rev. E* **74** 010602
- [55] Ulbrandt J G *et al* 2016 Direct measurement of the propagation velocity of defects using coherent x-rays *Nat. Phys.* **12** 794
- [56] Malik A *et al* 1998 Coherent x-ray study of fluctuations during domain coarsening *Phys. Rev. Lett.* **81** 5832–5
- [57] Fluerasu A, Sutton M and Dufresne E M 2005 X-ray intensity fluctuation spectroscopy studies on phase-ordering systems *Phys. Rev. Lett.* **94** 055501
- [58] Pierce M S *et al* 2009 Surface x-ray speckles: coherent surface diffraction from Au(001) *Phys. Rev. Lett.* **103** 165501
- [59] Shpyrko O G *et al* 2007 Direct measurement of antiferromagnetic domain fluctuations *Nature* **447** 68
- [60] Madsen A *et al* 2010 Beyond simple exponential correlation functions and equilibrium dynamics in x-ray photon correlation spectroscopy *New J. Phys.* **12** 055001
- [61] Li L *et al* 2014 Photon statistics and speckle visibility spectroscopy with partially coherent x-rays *J. Synchrotron Radiat.* **21** 1288–95
- [62] Hruszkewycz S O *et al* 2012 High contrast x-ray speckle from atomic-scale order in liquids and glasses *Phys. Rev. Lett.* **109** 185502
- [63] Wiegart L *et al* 2019 Instrumentation for in situ/operando x-ray scattering studies of polymer additive manufacturing processes *Synchrotron Radiat. News* **32** 20–7
- [64] Headrick R L *et al* 2018 Coherent x-ray measurement of step-flow propagation during growth on polycrystalline thin film surfaces *Nat. Commun.* **10** 2638
- [65] Lhermitte J R M 2015 Using Coherent X-Rays to Measure Velocity Profiles *PhD Thesis* McGill University, Montreal
- [66] Ament L J P *et al* 2011 Resonant inelastic x-ray scattering studies of elementary excitations *Rev. Mod. Phys.* **83** 705–67
- [67] Schlappa J *et al* 2012 Spin–orbital separation in the quasi-one-dimensional Mott insulator Sr₂CuO₃ *Nature* **485** 82
- [68] Hepting M *et al* 2018 Three-dimensional collective charge excitations in electron-doped copper oxide superconductors *Nature* **563** 374–8
- [69] Dvorak J *et al* 2016 Towards 10 meV resolution: the design of an ultrahigh resolution soft x-ray RIXS spectrometer *Rev. Sci. Instrum.* **87** 115109
- [70] Jarrige I *et al* 2018 Paving the way to ultra-high-resolution resonant inelastic x-ray scattering with the SIX beamline at NSLS-II *Synchrotron Radiat. News* **31** 7–13
- [71] Brookes N B *et al* 2018 The beamline ID32 at the ESRF for soft x-ray high energy resolution resonant inelastic x-ray scattering and polarisation dependent x-ray absorption spectroscopy *Nucl. Instrum. Methods Phys. Res. A* **903** 175–92
- [72] Kim J *et al* 2012 Magnetic excitation spectra of Sr₂IrO₄ probed by resonant inelastic x-ray scattering: establishing links to cuprate superconductors *Phys. Rev. Lett.* **108** 177003
- [73] Kim J *et al* 2014 Excitonic quasiparticles in a spin–orbit Mott insulator *Nat. Commun.* **5** 4453
- [74] Kitagawa K *et al* 2018 A spin–orbital-entangled quantum liquid on a honeycomb lattice *Nature* **554** 341
- [75] Ueda K *et al* 2018 Spontaneous Hall effect in the Weyl semimetal candidate of all-in all-out pyrochlore iridate *Nat. Commun.* **9** 3032
- [76] Kim J *et al* 2018 Quartz-based flat-crystal resonant inelastic x-ray scattering spectrometer with sub-10 meV energy resolution *Sci. Rep.* **8** 1958
- [77] Gog T *et al* 2013 Spherical analyzers and monochromators for resonant inelastic hard X-ray scattering: a compilation of crystals and reflections *J. Synchr. Rad.* **20** 74–9

- [78] Moretti Sala M *et al* 2018 A high-energy-resolution resonant inelastic x-ray scattering spectrometer at ID20 of the European Synchrotron Radiation Facility *J. Synchr. Rad.* **25** 580–91
- [79] Ishikawa D, Haverkort M W and Baron A Q R 2017 Lattice and magnetic effects on a d–d excitation in NiO using a 25 meV resolution x-ray spectrometer *J. Phys. Soc. Japan* **86** 093706
- [80] Huotari S *et al* 2017 A large-solid-angle x-ray Raman scattering spectrometer at ID20 of the European synchrotron radiation facility *J. Synchrotron Radiat.* **24** 521–30
- [81] Yavaş H *et al* 2019 Direct imaging of orbitals in quantum materials *Nat. Phys.* **15** 1–4
- [82] Chen-Wiegart Y-C K *et al* 2019 *Synchrotron Radiat. News* **32** accepted
- [83] Liu X *et al* 2019 Environmentally friendly Zr-based conversion nanocoatings for corrosion inhibition of metal surfaces evaluated by multimodal x-ray analysis *ACS Appl. Nano Mater.* **2** 1920–9
- [84] Sun K *et al* 2017 Operando multimodal synchrotron investigation for structural and chemical evolution of cupric sulfide (CuS) additive in Li-S battery *Sci. Rep.* **7** 12976
- [85] Deng J J *et al* 2018 Correlative 3D x-ray fluorescence and ptychographic tomography of frozen-hydrated green algae *Sci. Adv.* **4** eaau4548
- [86] Hong J *et al* 2019 Metal-oxygen decoordination stabilizes anion redox in Li-rich oxides *Nat. Mater.* **18** 256
- [87] Liu Y J *et al* 2016 Relating structure and composition with accessibility of a single catalyst particle using correlative 3-dimensional micro-spectroscopy *Nat. Commun.* **7** 12634
- [88] Tian Y Y *et al* 2019 Correlated multimodal approach reveals key details of nerve-agent decomposition by single-site Zr-based polyoxometalates *J. Phys. Chem. Lett.* **10** 2295–9
- [89] Liu D Y *et al* 2018 Identifying dynamic structural changes of active sites in Pt-Ni bimetallic catalysts using multimodal approaches *ACS Catal.* **8** 4120–31
- [90] Lo Y H *et al* 2019 Multimodal x-ray and electron microscopy of the Allende meteorite *Sci. Adv.* **5** eaax3009
- [91] Hingerl F F *et al* 2016 Characterization of heterogeneity in the Heletz sandstone from core to pore scale and quantification of its impact on multi-phase flow *Int. J. Greenhouse Gas Control* **48** 69–83
- [92] Smith E A *et al* 2014 Quantitatively imaging chromosomes by correlated cryo-fluorescence and soft x-ray tomographies *Biophys. J.* **107** 1988–96
- [93] Li Y *et al* 2015 Effects of particle size, electronic connectivity, and incoherent nanoscale domains on the sequence of lithiation in LiFePO₄ porous electrodes *Adv. Mater.* **27** 6591–7
- [94] Lim J *et al* 2016 Origin and hysteresis of lithium compositional spatiodynamics within battery primary particles *Science* **353** 566–71
- [95] Frenkel A I *et al* 2011 Combining x-ray absorption and x-ray diffraction techniques for in situ studies of chemical transformations in heterogeneous catalysis: advantages and limitations *J. Phys. Chem. C* **115** 17884–90
- [96] Li Y *et al* 2015 Complex structural dynamics of nanocatalysts revealed in operando conditions by correlated imaging and spectroscopy probes *Nat. Commun.* **6** 7583
- [97] Petoukhov M V and Svergun D I 2007 Analysis of x-ray and neutron scattering from biomacromolecular solutions *Curr. Opin. Struct. Biol.* **17** 562–71
- [98] Skar-Gislinge N and Arleth L 2011 Small-angle scattering from phospholipid nanodiscs: derivation and refinement of a molecular constrained analytical model form factor *Phys. Chem. Chem. Phys.* **13** 3161–70
- [99] Li X *et al* 2014 Direct visualization of the Jahn-Teller effect coupled to Na ordering in Na_{5/8}MnO₂ *Nat. Mater.* **13** 586–92
- [100] Park Y U *et al* 2017 In situ tracking kinetic pathways of Li⁺/Na⁺ substitution during ion-exchange synthesis of Li_xNa_{1.5-x}VOPO₄F_{0.5} *J. Am. Chem. Soc.* **139** 12504–16
- [101] Lin C-H *et al* 2019 Operando structural and chemical evolutions of TiS₂ in Na-ion and Li-ion batteries *Meet. Abstr. MA2019-01* 536
- [102] Zhao C *et al* 2019 Bi-continuous pattern formation in thin films via solid-state interfacial dealloying studied by multimodal characterization *Mater. Horiz.* **6** 1991–2002
- [103] Liu X *et al* 2019 Environmentally friendly Zr-based conversion nanocoatings for corrosion inhibition of metal surfaces evaluated by multimodal x-ray analysis *ACS Appl. Nano Mater.* **2** 1920–9
- [104] Cipriani F *et al* 2006 Automation of sample mounting for macromolecular crystallography *Acta Crystallogr. D* **62** 1251–9
- [105] Svensson O, Malbet-Monaco S, Popov A, Nurizzo D and Bowler M W 2015 *Acta Crystallogr. D* **71** 1757–67
- [106] Zander U *et al* 2015 MeshAndCollect: an automated multi-crystal data-collection workflow for synchrotron macromolecular crystallography beamlines *Acta Crystallogr. D* **71** 2328–43
- [107] Hirata K *et al* 2019 ZOO: an automatic data-collection system for high-throughput structure analysis in protein micro-crystallography *Acta Crystallogr. D* **75** 138–50
- [108] Bowler M W, Svensson O and Nurizzo D 2016 Fully automatic macromolecular crystallography: the impact of MASSIF-1 on the optimum acquisition and quality of data *Crystallogr. Rev.* **22** 233–49
- [109] Delageniere S *et al* 2011 ISPyB: an information management system for synchrotron macromolecular crystallography *Bioinformatics* **27** 3186–92
- [110] Fisher S J *et al* 2015 SynchWeb: a modern interface for ISPyB *J. Appl. Crystallogr.* **48** 927–32
- [111] Kiapour M H *et al* 2014 Materials discovery: fine-grained classification of x-ray scattering images *IEEE Winter Conf. on Applications of Computer Vision*
- [112] Huang H *et al* 2014 Diffusion-based clustering analysis of coherent x-ray scattering patterns of self-assembled nanoparticles *Proc. of the 29th Annual ACM Symp. on Applied Computing* (Gyeongju: ACM) pp 85–90
- [113] Wang B *et al* 2016 Deep learning for analysing synchrotron data streams 2016 *New York Scientific Data Summit (NYSDS)*
- [114] Meister N *et al* 2017 Robust and scalable deep learning for x-ray synchrotron image analysis 2017 *New York Scientific Data Summit (NYSDS)*
- [115] Wang B *et al* 2017 X-ray scattering image classification using deep learning 2017 *IEEE Winter Conf. on Applications of Computer Vision (WACV)*
- [116] Sahu P *et al* 2018 In-operando tracking and prediction of transition in material system using LSTM *Proc. of the 1st Int. Workshop on Autonomous Infrastructure for Science* (USA: ACM) pp 1–4
- [117] Guan X, Qin H, Yager K G, Choo Y and Yu D 2018 Automatic x-ray scattering image annotation via double-view Fourier-Bessel convolutional networks *British Machine Vision Conf.* pp 1–10
- [118] Yager K G *et al* 2017 Particulate matter contributions from agricultural tilling operations in an irrigated desert region *PLoS One* **10** e0138577
- [119] Liu J *et al* 2017 Healing x-ray scattering images *IUCrJ* **4** 455–65
- [120] Liu J and Yager K G 2018 Unwarping GISAXS data *IUCrJ* **5** 737–52

- [121] Ren F *et al* 2018 Accelerated discovery of metallic glasses through iteration of machine learning and high-throughput experiments *Sci. Adv.* **4** eaag1566
- [122] Xue D *et al* 2016 Accelerated search for BaTiO₃-based piezoelectrics with vertical morphotropic phase boundary using Bayesian learning *Proc. Natl. Acad. Sci. USA* **113** 13301–6
- [123] Chan E M *et al* 2010 Reproducible, high-throughput synthesis of colloidal nanocrystals for optimization in multidimensional parameter space *Nano Lett.* **10** 1874–85
- [124] Nikolaev P *et al* 2016 Autonomy in materials research: a case study in carbon nanotube growth *npj Comput. Mater.* **2** 16031
- [125] Noack M M, Yager K G, Fukuto M, Doerk G S, Li R and Sethian J A 2019 A Kriging-based approach to autonomous experimentation with applications to x-ray scattering *Sci. Rep.* **9** 11809
- [126] Chao W *et al* 2012 Real space soft x-ray imaging at 10 nm spatial resolution *Opt. Express* **20** 9777–83
- [127] Schroer C *et al* 2005 Hard x-ray nanoprobes based on refractive x-ray lenses *Appl. Phys. Lett.* **87** 124103
- [128] Mimura H *et al* 2007 Efficient focusing of hard x-rays to 25 nm by a total reflection mirror *Appl. Phys. Lett.* **90** 051903
- [129] Mimura H *et al* 2009 Breaking the 10 nm barrier in hard-x-ray focusing *Nat. Phys.* **6** 122
- [130] Cesar da Silva J *et al* 2017 Efficient concentration of high-energy x-rays for diffraction-limited imaging resolution *Optica* **4** 492–5
- [131] Conley R *et al* 2016 Multilayer Laue lens: a brief history and current status *Synchrotron Radiat. News* **29** 16–20
- [132] Huang X *et al* 2013 11 nm hard x-ray focus from a large-aperture multilayer Laue lens *Sci. Rep.* **3** 3562
- [133] Yan H *et al* 2018 Multimodal hard x-ray imaging with resolution approaching 10 nm for studies in material science *Nano Futures* **2** 011001
- [134] Huang X *et al* 2017 Hard x-ray scanning imaging achieved with bonded multilayer Laue lenses *Opt. Express* **25** 8698–704
- [135] Yan H *et al* 2017 Achieving diffraction-limited nanometer-scale x-ray point focus with two crossed multilayer Laue lenses: alignment challenges *Opt. Express* **25** 25234–42
- [136] Döring F *et al* 2013 Sub-5 nm hard x-ray point focusing by a combined Kirkpatrick-Baez mirror and multilayer zone plate *Opt. Express* **21** 19311–23
- [137] Vannoni M and Freijo-Martin I 2019 Installation and commissioning of the European XFEL beam transport in the first two beamlines from a metrology point of view *Rev. Sci. Instrum.* **90** 021701
- [138] Vivo A, Barrett R and Perrin F 2019 Stitching techniques for measuring x-ray synchrotron mirror topography *Rev. Sci. Instrum.* **90** 021710
- [139] Wang D-J *et al* 2019 Metrology for optical components of Taiwan Photon Source beamlines *Rev. Sci. Instrum.* **90** 021715
- [140] Sanchez Del Rio M *et al* 2016 DABAM: an open-source database of x-ray mirrors metrology *J. Synchrotron Radiat.* **23** 665–78
- [141] Rakitin M S *et al* 2018 Sirepo: an open-source cloud-based software interface for x-ray source and optics simulations *J. Synchrotron Radiat.* **25** 1877–92
- [142] Badami V G *et al* 2019 In situ metrology for adaptive x-ray optics with an absolute distance measuring sensor array *Rev. Sci. Instrum.* **90** 021703
- [143] Idir M *et al* 2010 X-ray active mirror coupled with a Hartmann wavefront sensor *Nucl. Instrum. Methods Phys. Res., Sect. A* **616** 162–71
- [144] Yumoto H *et al* 2006 At-wavelength figure metrology of hard x-ray focusing mirrors *Rev. Sci. Instrum.* **77** 063712
- [145] Wang H *et al* 2014 Fast optimization of a bimorph mirror using x-ray grating interferometry *Opt. Letters* **39** 2518–21
- [146] Kewish C M *et al* 2010 Reconstruction of an astigmatic hard x-ray beam and alignment of K-B mirrors fromptychographic coherent diffraction data *Opt. Express* **18** 23420–7
- [147] Wang H *et al* 2011 X-ray wavefront characterization using a rotating shearing interferometer technique *Opt. Express* **19** 16550–9
- [148] Matsuyama S *et al* 2012 Wavefront measurement for a hard-x-ray nanobeam using single-grating interferometry *Opt. Express* **20** 24977–86
- [149] Sutter J, Alcock S and Sawhney K 2012 In situ beamline analysis and correction of active optics *J. Synchrotron Radiat.* **19** 960–8
- [150] Kayser Y *et al* 2017 X-ray grating interferometer for in situ and at-wavelength wavefront metrology *J. Synchrotron Radiat.* **24** 150–62
- [151] Liu Y *et al* 2018 High-accuracy wavefront sensing for x-ray free electron lasers *Optica* **5** 967–75
- [152] Berujon S and Ziegler E 2016 X-ray multimodal tomography using speckle-vector tracking *Phys. Rev. Appl.* **5** 044014
- [153] Halbach K 1981 Physical and optical properties of rare earth cobalt magnets *Nucl. Instrum. Methods Phys. Res.* **187** 109–17
- [154] Yamamoto S *et al* 1992 *Rev. Sci. Instrum.* **63** 400–3
- [155] Tanabe T *et al* 1998 Development of an in-vacuum minipole undulator array for national synchrotron light source in-vacuum undulator *Rev. Sci. Instrum.* **69** 18–24
- [156] Hara T *et al* 2004 Cryogenic permanent undulators *Phys. Rev. Spec. Top. Accel. Beams* **7** 050720
- [157] Chubar O, Bengtsson J, Blednykh A, Kitegi C, Rakowsky G, Tanabe T and Clarke J 2013 *J. Phys.: Conf. Ser.* **425** 032005
- [158] Emery L and Borland M 2003 *Proc. of PAC 2003 paper TOPA014* p 256
- [159] Givord D, Li H S and Perrier de la Bâthie R 1984 Magnetic properties of Y₂Fe₁₄B and Nd₂Fe₁₄B single crystals *Solid State Commun.* **51** 857–60
- [160] Tanabe T *et al* 2009 *AIP Conf. Proc.* **1234** 29
- [161] Chao A W 1993 *Physics of Collective Beam Instabilities in High-Energy Accelerators* (Wiley: New York)
- [162] Gottschalk S C, Quimby D C and Kimura W D 2000 Gap-tapered undulators for high-photon-energy synchrotron radiation production *AIP Conf. Proc.* **521** 348–53
- [163] Sasaki S, Miyata K and Takada T 1992 A new undulator for generating variably polarized radiation *Jpn. J. Appl. Phys.* **31** L1794–6
- [164] Bahrtdt J *et al* 2008 *Proc. EPAC* pp 2222–4
- [165] Temnykh A B 2008 Delta undulator for Cornell energy recovery linac *Phys. Rev. Spec. Top. Accel. Beams* **11** 120702
- [166] Ganter R *et al* 2017 *Proc. FEL2017* p 125
- [167] Casalbuoni S *et al* 2018 *Proc. IPAC18* p 4223
- [168] Ivanyushenkov Y *et al* 2017 Development and operating experience of a 1.1 m-long superconducting undulator at the advanced photon source *Phys. Rev. Accel. Beams* **20** 100701
- [169] Moog E R, Dejus R J and Sasaki S 2017 Comparison of achievable magnetic fields with superconducting and cryogenic permanent magnet undulators—a comprehensive study of computed and measured values *Light Source Note: ANL/APS/LS-348 7/17*
- [170] Robin D *et al* 2002 *Proc. EPAC02* p 215